

# Exploring the Selection of Galaxy Clusters and Groups: An Optical Survey for X-ray Dark Clusters

David G. Gilbank<sup>1\*</sup> †, Richard G. Bower<sup>1‡</sup>, F. J. Castander<sup>2</sup> and B. L. Ziegler<sup>3‡</sup>

<sup>1</sup>*Department of Physics, University of Durham, South Road, Durham, DH1 3LE, UK*

<sup>2</sup>*Institut d'Estudis Espacials de Catalunya/CSIC Gran Capità 2-4, 08034, Barcelona, Spain.*

<sup>3</sup>*Sternwarte, Geismarlandstr. 11, 37083 Göttingen, Germany*

12 June 2018

## ABSTRACT

Data from a new, wide field, coincident optical and X-ray survey, the X-ray Dark Cluster Survey (XDCCS) are presented. This survey comprises simultaneous and independent searches for clusters of galaxies in the optical and X-ray passbands. Optical cluster detection algorithms implemented on the data are detailed. Two distinct optically selected catalogues are constructed, one based on I-band overdensity, the other on overdensities of colour-selected galaxies. The superior accuracy of the colour-selection technique over that of the single pass-band method is demonstrated, via internal consistency checks and comparison with external spectroscopic redshift information. This is compared with an X-ray selected cluster catalogue. In terms of gross numbers, the survey yields 185 I-band selected, 290 colour selected and 15 X-ray selected systems, residing in  $\sim 11\text{deg}^2$  of optical + X-ray imaging.

The relationship between optical richness/ luminosity and X-ray luminosity is examined, by measuring X-ray luminosities at the positions of our 290 colour-selected systems. Power law correlations between the optical richness/ luminosity versus X-ray luminosity are fitted, both exhibiting approximately 0.2 dex of intrinsic scatter. Interesting outliers in these correlations are discussed in greater detail. Spectroscopic follow up of a subsample of X-ray underluminous systems confirms their reality.

**Key words:** Galaxies: clusters: general, X-rays: galaxies: clusters, Surveys, Cosmology: miscellaneous

## 1 INTRODUCTION

Clusters of galaxies are extremely important astrophysical tools. They are the most massive virialised objects in the Universe. Since clusters form from extremely high peaks in the initial density field on scales of around  $10 h^{-1}\text{Mpc}$ , they are sensitive to the amplitude of the power spectrum on these scales. Thus, observations of the cluster mass function out to large redshifts can place tight constraints on cosmological parameters (e.g.  $\Omega_m$ ,  $\sigma_8$ ,  $\Lambda$ ; Eke et al. 1996). They are also powerful laboratories for studying galaxy formation and evolution. Several different techniques exist for finding clusters, each relying on different properties of clusters in order to locate them, and it is important to try to understand how the selection method may bias the sample and affect the scientific results.

The first attempt at a large, homogeneous survey for galaxy clusters was conducted by Abell (1958). This was a phenomenal effort by one individual to identify overdensities of galaxies

by visual inspection of Palomar Observatory Sky Survey (POSS) photographic plates, yielding nearly 1700 clusters in his “homogeneous statistical sample” and over 2700 in his full sample. Similar catalogues were constructed by Zwicky and collaborators (Zwicky & et al. 1968). Abell (1958)’s Northern catalogue was extended to the Southern hemisphere by Abell et al. (1989), applying his same statistical criteria.

With the advent of space-based X-ray telescopes, such as UHURU, a new way to discover galaxy clusters was found. Spatially extended, thermal X-ray emission was detected and shown to be due to the hot intracluster medium (ICM) - the plasma trapped in a cluster’s potential well (Mitchell et al. 1976; Serlemitsos et al. 1977). This provided a way to show that the cluster was a genuine physically bound system. Furthermore, the background signal (produced by X-ray point sources) is lower in the X-ray sky than the background in the optical, produced by a much greater surface density of foreground and background galaxies. Optical selection techniques lost favour: their main disadvantage being that there was no way, at the selection stage, to distinguish between genuine clusters and chance projections of less massive galaxy groups along the lines of sight. Extensive discussions of this contamination have

\* Email: D.G.Gilbank@durham.ac.uk

† Visiting astronomer of the German–Spanish Astronomical Center, Calar Alto, operated by the Max–Planck–Institut für Astronomie, Heidelberg, jointly with the Spanish National Commission for Astronomy.

been published (e.g. Katgert et al. 1996; van Haarlem et al. 1997). To reject such spurious systems, observationally expensive spectroscopy is required to confirm the overdensities in 3D. Despite the revolutionary new X-ray techniques, four large optical photographic cluster surveys with follow up spectroscopy were undertaken in the late 1980s (Gunn et al. 1986; Couch et al. 1991; Maddox et al. 1988; Lumsden et al. 1992). The first two used visual inspection of photographic plates, and the second two utilised machines which automatically measured parameters of objects from photographic plates. The catalogues derived from plate scanning could be passed to computerised overdensity detection algorithms, and for the first time cluster detection advanced beyond subjective visual inspection.

Prior to the construction of large X-ray selected samples of clusters, it was natural to target the optically selected clusters described above with X-ray telescopes in an attempt to measure the X-ray luminosity function (XLF) at high redshift. Castander et al. (1994) used ROSAT to observe cluster candidates in the redshift range 0.7-0.9 from a 3.5 square degree subsample of Gunn et al. (1986)'s optical cluster catalogue and also found surprisingly weak X-ray emission ( $\approx 10^{43}$  erg s $^{-1}$ ). Bower et al. (1994) undertook ROSAT X-ray observations of optically selected clusters from the Couch et al. (1991) catalogue (Couch et al. 1991 visually selected clusters based on the density enhancement of galaxies above the mean background, but tested their method exhaustively against simulated data). From this 46 deg $^2$  catalogue, Bower et al. (1994) took clusters with reliable spectroscopic follow up and X-ray data in the redshift range 0.15 to 0.66, assuming this to be a random subsample of the full catalogue. The total sky coverage of this survey was 26.8 deg $^2$  and contained 14 clusters. The X-ray luminosities of all but two of the clusters was found to be surprisingly weak - less than  $5 \times 10^{43}$  erg s $^{-1}$ . This decrease with respect to the locally measured value was attributed to evolution in the XLF between  $z=0$  and  $\approx 0.4$ . The alternative is that if the XLF does not evolve between these redshifts, then the missing X-ray luminous clusters must be made up of optically poorer systems, missing from this sample. This raises the question *do optical and X-ray surveys sample the same clusters?*

With the advent of high quantum-efficiency, large format charged-coupled devices (CCDs) in the early 1990s, optical cluster studies are again becoming attractive. The first serious attempt at an automated optical CCD survey with a quantifiable selection function was carried out with the Palomar Distant Cluster Survey (PDCS, Postman et al. 1996). Their pioneering work involved assuming a model for the spatial and luminosity distribution of galaxies in a cluster and in the field, and filtering the data using these models as templates. Using a likelihood analysis of the data, with cluster richness and redshift as free parameters, the most likely cluster candidates could be extracted, and their redshifts estimated as a by-product of the process. The technique is known as the matched-filter (MF) and is discussed in more detail in §3. This method reduced spurious clusters due to projection effects compared with the more traditional techniques described above, but many still remained (discussed further below). The MF need only be used on photometric data from a single passband, but with an additional filter other techniques are possible. Algorithms using colour selection have been proposed (e.g. Gal et al. 2000; Gladders & Yee 2000). Gal et al. (2000) used mild colour cuts to reduce contamination due to field-like galaxies. Since elliptical galaxies are predominantly found in dense environments (the morphology-density relation, Dressler 1980), and exhibit only a narrow range of colours at a given redshift, in any

environment, data can be filtered in colour to remove galaxies with colours incompatible with ellipticals. Gladders & Yee (2000) took the colour selection a stage further, placing very strict colour cuts in two-colour data, to only search for overdensities of galaxies with colours consistent with elliptical galaxies at a given redshift (see §3). This works because in all known clusters for which multi-band photometry exists (regardless of how the cluster was selected), a tight relation exists between the colour and magnitude of its early-type galaxies (e.g. Visvanathan 1978; Bower et al. 1992). This relation is clearly visible over small spatial scales ( $\sim$  the size of the cluster core), as early-type galaxies are predominantly found in the central regions of a cluster (Dressler 1980).

With an abundance of new wide-field optical and X-ray (Jones et al. 1998; Vikhlinin et al. 1998; Mason et al. 2000; Romer et al. 2000) imaging data, it is timely to directly compare clusters found using these different methods. To recap, X-ray selected clusters are required to have a hot, dense intracluster plasma; whereas optical selection just requires an overdensity of galaxies. To this end, we have undertaken optical and X-ray imaging surveys in exactly the same regions of sky. We refer to this as the X-ray Dark Cluster Survey (XDCS), as the project is specifically aimed at searching for the optically rich but X-ray underluminous clusters described in Bower et al. 1994, Bower et al. 1997.

A plan for the outline of this paper is as follows. The X-ray field selection, optical observations and data reduction are presented in §2. Two optical cluster detection algorithms are presented in §3, the first uses only single band optical photometry, and is a variant of the now widely-used Matched Filter algorithm (Postman et al. 1996); the second utilises colour information, and is our implementation of the algorithm of Gladders & Yee 2000. §4 discusses measures of optical richness, and the construction of the optical catalogues. §5 deals with the X-ray selection of clusters. These samples are cross-compared with the X-ray sample in §6. Spectroscopic follow up for a subsample of X-ray underluminous clusters is presented in §7, and finally our conclusions in §8.

## 2 THE X-RAY DARK CLUSTER SURVEY

### 2.1 Sample Selection and Observations

X-ray imaging is observationally expensive. Thus we chose to base our survey on archival X-ray data, which is relatively inexpensive to follow-up with wide-field optical imaging. Essentially a random sample of deep extragalactic X-ray fields was required. The ROSAT International X-ray/ Optical Survey (RIXOS, Mason et al. 2000) provided an ideal list of such fields. Their sample was constructed from ROSAT Position Sensitive Proportional Counter (PSPC) fields which had exposure times of at least 8ks. This ensures that sources at the intended survey flux limit (for a point source) of  $3 \times 10^{-14}$  erg cm $^{-2}$  s $^{-1}$  (0.5-2.0 keV) lie significantly above the sensitivity threshold of every field. They also limited the choice of fields to those which have Galactic latitudes greater than 28 $^\circ$  in either hemisphere, since RIXOS is primarily intended for extragalactic source studies.

The archival ROSAT fields listed in Table 1 were observed in the optical using the Wide Field Camera (WFC) on the Isaac Newton Telescope (INT), La Palma. The observations were carried out in two runs, in June 1998 and January 1999. The median seeing for the two runs was around 1.0'' and 1.6'' respectively. Conditions for both runs were photometric. The inner  $\gtrsim 19$  arc minutes of the PSPC fields were imaged to depths of  $V \sim 24$  and  $I \sim 23$  (50% completeness). This is the region of the PSPC used for X-ray source

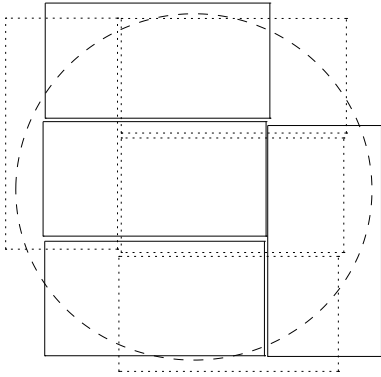


**Figure 1.** INT WFC Tiling Strategy. The circle represents the inner 19 arcmin radius of the PSPC field. Rectangles show the four CCDs of the WFC. Solid lines indicate the camera configuration in one orientation and broken lines show the camera rotated through  $180^\circ$ . The diagram illustrates how the field can be efficiently imaged in two pointings.

identification in RIXOS, to ensure the best X-ray image quality and the most accurate source positions (Mason et al. 2000). For each band, two exposures were taken, rotating the camera through 180 degrees, and offsetting the centre of the pointing in order to ensure optimum coverage of the PSPC, as shown in Fig. 1. Hereafter, images taken with the camera rotator angle set to 0 degrees will be referred to as *A* images; and those with a rotator angle of 180 degrees *B* images. The two independent observations of a large fraction of the survey area will provide important internal checks of galaxy photometry and of cluster catalogues generated from independent data covering the same area of sky. We shall use the term “mosaic” to refer to a single pointing (either *A* or *B*) comprising the four WFC chips.

The WFC comprises four thinned EEV ( $2048 \times 4100$ ) Charge-Coupled Device (CCD) chips, at the prime focus of the 2.5 metre INT. The science devices have 13.5 micron pixels ( $0.333''/\text{pixel}$ ). Each covers an area of  $22.8 \text{ arcmin} \times 11.4 \text{ arcmin}$  on sky. The total sky coverage per exposure is 0.29 square degrees. A single exposure covers 76% of the ROSAT PSPC area. By using two exposures, virtually the entire inner 38 arc minute diameter was covered: see Fig. 1.

## 2.2 Optical Data Reduction

The data reduction was carried out using mostly standard IRAF<sup>1</sup> routines, and is detailed below.

### 2.2.1 Debiasing and Linearity Correction

Bias frames were visually inspected for quality. Master bias frames were constructed for each night by taking the mean of all the good data using ZEROCOMBINE. Next it was necessary to correct for the non-linear response (due to problems with the ADC) of the WFC. This was achieved by applying polynomial corrections taken from the Cambridge Wide Field Survey (WFS) webpage (<http://www.ast.cam.ac.uk/~wfcSUR/>). The temporally nearest fits were used. The August 1998 polynomials were used for the XDCS data taken in June 1998 and the October 1998

values for January 1999 data (the non-linearity was found to remain stable between October 1998 and August 1999). Following this correction, the camera residual non-linearity is estimated by the WFS team to be less than 0.5% of the sky level.

### 2.2.2 Flatfielding and Defringing

Flatfielding was carried out using master flats for each night. These were constructed from a median combination of all the science data in the V-band and from twilight sky flats in the I-band. The I-band science data were not used to construct master flatfields as the thinned CCDs suffer from fringing. The fringing patterns are additive, but their broad structure is largely stable with time. Therefore, all the I-band data for each chip were averaged together to make master fringe frames for each night. Although the shape of the lines is stable, the amplitude can vary considerably (although always at the level of a few percent of sky). Thus, a method was needed to scale the amplitude of the fringe mask to the amplitude of the fringes in each data frame, before subtraction. This was done with software kindly provided by Mike Irwin. The scaled fringe masks were then subtracted from the I-band science images. After this procedure the level of fringing is reduced to  $\sim 0.5$  percent of sky, which is of the order of the residual non-linearity.

### 2.2.3 Object Detection and Photometry

The SExtractor package (Bertin & Arnouts 1996) v2.2.1 was used to locate and classify objects in the optical data. Firstly the seeing was measured for each frame. This was accomplished by fitting Gaussian PSFs to all bright ( $> 10\sigma$ ) detections, classified by SExtractor as stars.

SExtractor was run in double image mode on each pair of aligned V/I images using the V-band image as the detection image, and the I-band as the measurement image. This was done in order to obtain SExtractor MAG\_BEST magnitudes to measure the total magnitude for I-band objects. Ideally one would like to use the redder passband for object detection as the number counts are shallower for redder bands (i.e. a lower background for cluster detection), but it was found that the residual fringing in the I-band posed a problem for object detection in a few frames, dramatically increasing the numbers of false detections in the most badly-fringed frames. Although the level of the remaining fringes is too small to affect the photometry (the photometric error is still dominated by the linearity correction at the bright end, and Poisson noise at the faint end), the background estimation method used by SExtractor cannot model the fringes. High residuals pass above the SExtractor detection threshold and are classified as extended objects. As this method could not be reliably used on all the data, its use was decided against. The depth of the data is such that, by limiting the object catalogues to  $I = 22.5$ , few objects are missed which would have been detected in the I-band image (see magnitude limits in Fig. 6) and the use of the V-band to perform detection is entirely one of operational ease. The survey is therefore I-band limited.

After generating a list of object positions from SExtractor the *x* and *y* coordinates of objects in the V frame were logged and used to position the aperture for photometry. For each V/I frame pair, the frame with the better seeing was convolved to that of the worst, using Gaussian convolution. The IRAF task `phot` was used to perform aperture photometry to measure colours, using an aperture of diameter  $2.6 \times$  the seeing (e.g. Lilly et al. 1991), on the aligned, convolved V and I frames.

<sup>1</sup> IRAF is distributed by the National Optical Astronomy Observatory which is operated by AURA Inc. under contract with the NSF.

**Table 1.** List of ROSAT Fields in XDCS Columns give: RIXOS ID of field; name of the target of the original ROSAT pointing; RA, Dec; exposure time of field in RIXOS survey; overlapping X-ray cluster survey (V - VMF, S - SHARC); exposure time of the VMF or SHARC pointing (to give an indication of the depth to which they could have searched for X-ray emission).

RIXOS ID	Target	$\alpha$ (J2000) [hh:mm:ss.s]	$\delta$ (J2000) [dd:mm:ss]	$T_{exp}$ (ks)	Overlapping Survey	$T_{exp}(\text{overlap})$ (ks)
R110	LHS 2924	14:28:43.17	+33:10:45.47	18.3	V	28.5
R116	NOWER2	12:03:60.00	+56:10:11.99	30.1	—	—
R122	Meaty	16:29:24.00	+78:04:48.01	38.5	S	34.4
R123	1116+215	11:19:4.80	+21:18:36.00	25.0	V	32.2
R126	ON 231	12:21:33.60	+28:13:48.00	10.4	V	12.5
R133	CY UMA	10:56:55.20	+49:42:0.00	9.4	V	7.9
R205	P100578	23:12:21.60	+10:46:48.00	10.3	S	9.8
R211	S5 0716+7	07:21:52.70	+71:20:23.99	21.0	S	17.3
R213	IRAS 0759	08:04:31.20	+65:00:0.00	8.4	V	6.4
R216	S4 0917+6	09:21:36.00	+62:15:35.99	19.5	V	15.9
R217	1411+442	14:13:48.00	+44:00:0.00	25.3	V	22.5
R220	RX J1726.	17:26:12.00	+74:31:11.99	10.6	V	8.1
R221	E0845+378	08:48:19.20	+37:40:11.99	12.4	V	10.0
R223	CM DRA	16:34:24.00	+57:09:0.01	47.5	V	37.3
R224	HZ43	13:16:24.00	+29:06:0.00	34.9	S	18.3
R227	GD140	11:36:33.51	+29:47:60.00	33.9	V	26.6
R228	GBS0839+3	08:38:47.90	+36:31:12.00	11.0	V	9.2
R231	Survey Fi	10:10:16.70	+54:45:0.00	16.8	V	14.4
R236	Q1700+515	17:01:23.90	+51:49:12.00	8.2	V	6.5
R245	H0323+022	03:28:25.82	+02:47:57.84	25.7	S	24.5
R248	3C216	09:09:33.50	+42:54:0.01	23.6	V	19.9
R254	MRK 273	13:44:43.10	+55:53:24.00	17.1	V	28.1
R255	0755+37	07:58:28.70	+37:47:24.00	16.0	S	15.5
R257	B2 0902+3	09:05:31.10	+34:07:48.00	14.5	V	26.5
R258	1115+080	11:18:16.70	+07:46:12.00	14.4	V	13.2
R262	520	01:24:33.50	+03:47:60.00	13.9	V	12.0
R265	B2 1308+3	13:10:28.70	+32:20:59.99	13.0	V	7.6
R268	MRK 463	13:56:2.30	+18:22:12.00	11.6	V	18.3
R272	3C 371	18:06:50.40	+69:49:12.00	10.5	S	8.0
R273	1040+123	10:42:45.51	+12:03:36.00	10.2	V	8.4
R274	1404+226	14:06:21.60	+22:23:60.00	10.1	V	6.7
R278	MKN 789	13:32:24.00	+11:06:36.00	9.6	V	9.1
R281	III ZW2	00:10:28.70	+10:58:12.00	9.1	V	16.8
R283	1H 0414+0	04:16:52.70	+01:05:24.00	9.0	—	—
R285	PSR 0940+	09:43:43.20	+16:31:12.00	9.0	V	8.1
R287	MKN 40	11:25:36.00	+54:22:48.00	8.8	V	7.7
R292	GLIESE 70	01:43:21.50	+04:19:48.00	8.7	V	5.4
R293	GD 90	08:19:47.90	+37:31:12.00	9.0	V	7.3
R294	KUV 2316+123	23:18:45.0	+12:36:00.00	9.5	—	—

Objects with a SEXTRACTOR CLASS\_STAR index of  $\leq 0.90$  were taken to be galaxies. Detections with FLAGS $\geq 4$  were rejected. This means blended objects and those with near neighbours are kept, but those with saturated pixels, or corrupted data (e.g. due to boundary effects) are rejected.

#### 2.2.4 Photometric Calibration

The photometric data were converted to the standard Cousins system using observations of several Landolt (1992) standard star fields each night. Due to the small size of these fields, only the central chip sampled the standard stars well. Therefore an internal calibration of the other three chips to the reference central chip was performed by comparing the relative sky levels in the chips for each observation. The flux difference was then converted into a relative magnitude offset. Different offsets were measured for each run, due to servicing of the instrument between the two runs, which changed the gains of the devices. The uncertainty on the absolute calibration

derived from the scatter between Landolt stars, and repeat observations of the same fields was estimated to be better than 0.1 mags.

#### 2.2.5 Astrometric Calibration

Relative astrometry between the chips was performed by Mark Taylor in Cambridge using A and B observations of one of our fields. This gives an internal astrometric solution converting chip coordinates into global camera coordinates. This solution is available on the WFS webpage. A precise external astrometric calibration is not essential, as clusters are very extended objects, so specifying a cluster centre to within several arcseconds is sufficient. Therefore, the pointing position of the telescope was used as the centre of the instrument and the internal solution described was used to transform chip coordinates to sky coordinates. This gives an external accuracy of around 3 arcseconds or better, but the internal accuracy is better than 0.5 arcseconds. For the purpose of cluster detection it

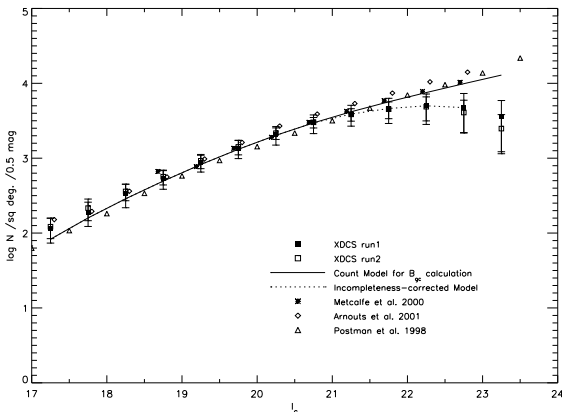


**Figure 2.** I-band galaxy counts for both XDCS runs and model counts used in derivation of  $B_{gc}$ . Error bars are standard deviation from field to field. Both runs are found to be in good agreement, suggesting that the photometry for XDCS is homogeneous. Overplotted is the completeness model (relative to Metcalfe et al. 2001) used to allow data to  $I = 22.5$  to be used. Magnitudes are SEXTRACTOR MAG\_BEST magnitudes. I-band counts from the literature are overplotted, and found to be in good agreement. The completeness is modelled by a single-sided Gaussian of width 1.90 mags, centred on  $I = 20.86$ .

is the relative positions between galaxies (i.e. the internal solution) that is important.

### 3 OPTICAL CLUSTER DETECTION ALGORITHMS

Two different cluster detection methods were applied to the optical data. Both use positional information to search for overdensities in the galaxy catalogues, but they do this in different ways. The first uses only the I-band photometry, and looks for overdensities of galaxies which appear to follow the luminosity function of a galaxy cluster; the second includes the V-band data and uses the V-I colour to search for the colour-magnitude relation of early-type cluster galaxies.

#### 3.1 The Matched Filter Algorithm

The “matched-filter” (MF) was pioneered by Postman et al. 1996, and modified by several groups including Kawasaki et al. (1998); Kepner et al. (1999); Lobo et al. (2000). Its principle is to assume that galaxy clusters follow some well-defined model, in both their spatial and luminosity distributions. i.e. some universal radial profile is assumed for the distribution of galaxies in a cluster, which can be projected into 2D. In the same way, some universal luminosity function can be assumed for its member galaxies. High resolution N-body simulations suggest that virialised objects follow a universal density profile (NFW Navarro et al. 1997); observations show that cluster profiles are compatible with such a profile, but also with simpler analytic fits (Carlberg et al. 1997; Lubin & Postman 1996). The luminosity function of galaxies in clusters and the field is well-fitted by a Schechter function with mild luminosity evolution (Yee & López-Cruz 1999), or mild luminosity and density evolution (Lin et al. 1999). This model can be scaled to any redshift. The observed radial profile scales with redshift according to the angular diameter distance,  $D$ , to the object, given by

$$D = (c/H_0)\{q_0z + (q_0 - 1)[(2q_0z + 1)^{1/2} - 1]/q_0^2(1+z)^2\} \quad (1)$$

where  $c$  is the velocity of light,  $H_0$  is the Hubble constant,  $q_0$  is the deceleration parameter, and  $z$  is the redshift<sup>2</sup>. The observed luminosity distribution scales according to the distance modulus formula  $m - M = 5 \log(d_{Mpc}) + 25 + k + e$  with corrections for bandpass shifting due to the redshift of the source ( $k$ -correction,  $k$ ) and evolutionary corrections of the stellar populations ( $e$ ).  $m$  and  $M$  are the apparent and absolute magnitudes of the galaxy, and the luminosity distance,  $d$ , in Mpc is a factor of  $(1+z)^2$  times the angular diameter distance,  $D$ . The only other free parameter the model needs is the *richness* of the cluster (i.e. some parameterisation of the number of galaxies it contains). Thus, a model for the observed properties of a galaxy cluster of arbitrary richness and redshift is obtained. The final aspect to be taken into account is the distribution of field galaxies. This model can be derived from the data itself. It is assumed they are randomly distributed in position - explicitly ignoring the correlation between the positions of pairs of galaxies (see §3.1.4). The contribution of cluster galaxies to the total number of galaxies in any dataset will be small, unless the survey consists of small fields targeted at clusters. Hence, by studying the number density and luminosity distribution of the whole sample, a model for the field galaxies can be deduced. The luminosity function in the PDCS method had to be modelled by a power-law due to assumptions made in the derivation (see paper for details) which is generally a good fit to the data, depending on the magnitude range observed (e.g. Metcalfe et al. 2001, Smail et al. 1995, see also Fig. 2).

Astronomical data comprising positions and photometry can be searched for regions where the likelihood of the data fitting this cluster+field model is high. Since the cluster model is a function of richness and redshift as a by-product of the detection process, a most likely richness and redshift for each cluster candidate is obtained as a by-product.

The Postman et al. 1996 algorithm made several approximations (detailed in their paper) which have been removed and treated more fully by later workers. For example, their main approximation was to assume that the data (galaxies) could be binned in both position and magnitude in such a way that each bin had sufficient datapoints that their distribution was Gaussian. This was replaced by a more general treatment which assumed Poisson distribution of the data by Kawasaki et al. (1998). The other key assumption which has been followed by all subsequent works until Lobo et al. (2000) is that the models predict a unique combination of spatial and luminosity distributions at a given redshift. The drawback of this approach is that if a cluster is slightly larger or smaller in angular extent than predicted for its luminosity distribution, its signal is reduced and the probability of detection lessened. Lobo et al. (2000) circumvented this problem by choosing the combination of spatial and luminosity profiles which independently maximised the signal.

<sup>2</sup> Throughout we assume  $H=64\text{km s}^{-1}\text{Mpc}^{-1}$ ,  $q_0 = 0.1$  unless otherwise stated. This is to provide consistency with the stellar population synthesis models made available to us. Adopting the currently favoured cosmological parameters of:  $\Omega_m = 0.3$ ,  $\Omega_\Lambda = 0.7$  and  $H_0 = 70 \text{ km s}^{-1}$  would affect the derived luminosities by  $\lesssim 4\%$  and inferred linear sizes by  $\lesssim 2\%$  over the redshifts considered.

### 3.1.1 A New Matched-Filter Algorithm

The algorithm presented here is closest in spirit to the technique of Lobo et al. (2000), in that the assumptions for the distributions in radial profile and luminosity have been decoupled. This method offers many advantages for this project, the main one being that it is unnecessary to assume a characteristic physical size for the model cluster, *a priori*, which will obviously help if unrelaxed systems have larger angular extent than virialised systems of the same richness and redshift (as may intuitively be expected). This also offers some computational rewards which will be explained below.

The assumptions for this model are:

- Field galaxies are distributed randomly over the sky (the two point galaxy-galaxy correlation function is explicitly ignored), and that their magnitude distribution has the same shape throughout the survey but changes slightly in normalisation, from field to field (see Fig. 2).

All magnitudes in this section refer to the I-band. In principle any photometric passband can be used, but as red a band as possible is desired. This is due to the fact that the field galaxy counts steepen toward shorter wavelengths, so the contrast between the cluster and the field is greater at longer wavelengths (e.g. power-law slopes of 0.28 and 0.40 were measured in the I- and V-bands, respectively, by Smail et al. 1995).

- Galaxy clusters appear as overdensities in this background distribution, and their visibility can be enhanced by filtering the galaxy catalogue with a Gaussian filter, the size of which is given by the typical sizes of galaxy clusters from the literature.

- Galaxy clusters follow a Schechter (Schechter 1976) Luminosity Function (LF), with fixed faint-end slope, and the normalisation is given by the amplitude of the overdensity (i.e. the cluster's richness). The typical apparent magnitude  $m^*$  of the LF is a function of redshift.

The maximum-likelihood estimator,  $C$ , of Cash (1979) is then applied to the data.

### 3.1.2 Implementation

The algorithm was run on each mosaic separately. First, filtering of the spatial information was performed. The  $x$  and  $y$  positions of galaxies brighter than magnitude 22.5 were read in, and the mosaic filtered with five Gaussian filters of different widths. The standard deviation of each filter was taken from Lobo et al. (2000). The widths shall be referred to as  $W_n$  for the  $n^{\text{th}}$  filter (to avoid confusion with standard deviation  $\sigma_s$ , later), but are equivalent to the  $\sigma_{ang}$  in their paper. The widths,  $W_1, \dots, W_5$ , ranged from  $\sim 0.35$  to  $\sim 1.42$  arcmins in steps of  $\sqrt{2}$ , these represent the typical core-widths of clusters in the redshift range  $\approx 0.2$  to 1.0. A cut-off radius of  $3 W_n$  is used. Unlike Lobo et al. (2000), instead of using a regular grid, the positions of the galaxies themselves were used as the grid to centre each of the Gaussian filters. This adaptive-grid method was also adopted by Kepner et al. (1999) and has the advantage that it ensures adequate resolution in the core of a cluster, and saves computational expense by performing few calculations where the galaxy density is low. For each spatial filter the mean and standard deviation of the filter amplitude was calculated (the amplitude follows a Gaussian distribution), and all five filters normalised onto the same system (by subtracting the mean and dividing by the standard deviation).

Peaks were then found in each filter, by sorting the list of signal amplitudes, retaining the highest value, and then searching down the list, removing detections which fell within a radius  $W_n$  of

the peak, and retaining the next highest value which did not. Values lower than a minimum threshold of  $2.5 \sigma$  were immediately rejected.

The peaks from the five filters were then sorted and cross-correlated. If a peak was detected in more than one filter, the highest amplitude was retained and the duplicate detections removed. Two peaks were considered to be the same object if the distance between them was less than the mean of their scales (i.e.  $(W_n + W'_n)/2$ ) (Lobo et al. 2000). This resulted in a single list of peaks, each with an associated scale (the filter width,  $W_n$ , in which the highest signal was detected).

A richness estimate of the candidate was then required, for use in the maximum-likelihood estimation. As a first pass estimate, the number of galaxies within a fixed angular radius was taken, for all candidates, regardless of its associated  $W_n$ . (The decision to use a fixed angular search cell is explained below.) This number then had the number of background galaxies, scaled to the same area, subtracted from it. The background galaxy density was found by counting the number of galaxies in an annulus of radius  $3 \times W_n$  to  $15 \times W_n$ . The  $W_n$  value was used to ensure the annulus is sufficiently far from the cluster core to avoid contamination with cluster members.

The importance of using a local estimate of the background can be seen by looking at the field to field variations in our data in the number counts in Fig. 2. These variations are due to a combination of residual offsets in the photometric calibration and intrinsic cosmic variance. The local background number density was also used to re-normalise the expected number counts locally, for use in the maximum-likelihood calculation. The cumulative counts were used at  $I=20.5$ , two magnitudes brighter than the limiting magnitude, to ensure both a high number of objects and high completeness.

In estimating galaxy number densities, the geometry of the mosaic field needed to be taken into account. To compensate for border effects, where the detect cell starts to fall off the edge of the field, a weighting function was constructed, taking account of the fraction of the detect cell area lost. This requires caution, as upweighting the signal from a few galaxies is likely to result in increased spurious detections, due to the uncertainty from using fewer galaxies. Thus a cut was made, rejecting candidates where the fraction of the area lost to borders is  $> 0.20$ .

The Cash  $C$  statistic (below) was then applied to the data within a radius of  $2.5 \times W_1$ . Most other MF algorithms use a search radius fixed in physical units at the estimated redshift of the cluster, and Lobo et al. (2000) use the radius which maximises the signal. Early experimentation with simulated clusters showed that just using data within a fixed radius (of the smallest filter) was adequate and this is done for the sake of simplicity and computational speed. Since the same galaxies always enter the maximum-likelihood calculation, this makes the calculation much more stable. It also meant that a fair estimate of the likelihood could be found by a simple application of the Cash statistic, without recourse to bootstrap re-sampling the detections to determine their significance, as needed by the Lobo et al. (2000) method.

The results were sorted in order of increasing  $C$  (decreasing likelihood), and overlapping detections removed using a 2D friends-of-friends groupfinding algorithm (Huchra & Geller 1982). The groupfinder started with the most significant point and searches within a fixed radius (the linking length) for another point. If a point was found, then the search was repeated within the same radius around this new point. The search continued, linking all points within the linking length of a neighbour, until no more points could

be linked. Thus only the most significant candidate was retained and all linked neighbours were removed. This method was found to work better than just removing candidates within a fixed radius of each other, as this latter approach tended to either remove too many (unassociated) candidates (if the rejection radius was too large) or leave multiple detections of the same candidate around the periphery of a rich candidate. The friends-of-friends algorithm is a more natural method for associating related points. Through experimentation on fields with known clusters, a linking length of 500 pixels ( $\sim 2.8$  arcmin) appeared optimal. Finally, the distance between the highest likelihood point (the candidate centre) and the most distant point from it joined to the group was recorded. This distance was then used as a characteristic radius to estimate the extent of the group. This will be important later for matching up overlapping candidates.

### 3.1.3 Maximum-Likelihood Estimation

Cash (1979) originally developed the maximum-likelihood method for application to general Poissonian problems (see original paper for full details). The Cash statistic,  $C$ , is given by equation 2.

$$C = 2 \left( E - \sum_{i=1}^n \ln I_i \right) \quad (2)$$

For the application here,  $E$  is the expected number of galaxies per unit area per unit luminosity. The number of galaxies can be broken up into cluster and field. Now, observing over a given area and luminosity range on the sky,  $E = E(\theta, m; z_c)$  where  $\theta$  is the angular radius of the search area,  $m$  is the galaxy magnitude, and  $z_c$  is the redshift of the cluster. Thus the number expected within these spatial and luminosity ranges is:

$$E = \int_0^{m_{lim}} [\Lambda \phi_{cl}(m) + b(m)] d\Omega dm \quad (3)$$

and

$$I_i = [\Lambda \phi_{cl}(m_n^i) + b(m_n^i)] d\Omega dm \quad (4)$$

where each  $i$  is a data point.

$d\Omega$  and  $dm$  are elements of solid angle and magnitude, respectively. In most MF algorithms this is modelled as a power-law, as is necessary in Postman et al. 1996 original implementation. However, there is no reason to assume this model in our maximum-likelihood approach, and so the background number counts were taken from the data, with a model for incompleteness, relative to literature counts, and a local normalisation (explained above).  $b(m)$  is the model for the field galaxy counts, as a function of magnitude;  $\phi_{cl}(m)$  is a model for the cluster contribution. The lower limit of the integral was replaced with  $I=16$  in practice, as saturation sets in around this point, and there are so few galaxies this bright within the whole survey that number counts could not reliably be computed.  $\Lambda$  is a parameterisation for the richness of the cluster, such that the number of cluster galaxies  $n_c = \Lambda \phi_{cl}$ , with  $\Lambda$  normalised by

$$\int_0^{m_{lim}} \Lambda \phi_{cl}(m) dm = 1 \quad (5)$$

The luminosity distribution,  $\phi_{cl}$ , can be modelled by the Schechter function (Schechter 1976):

$$\phi_{cl}(m) = 0.92 \phi^* \exp\{-0.92(\alpha+1)(m-m^*) - \exp[-0.92(m-m^*)]\} \quad (6)$$

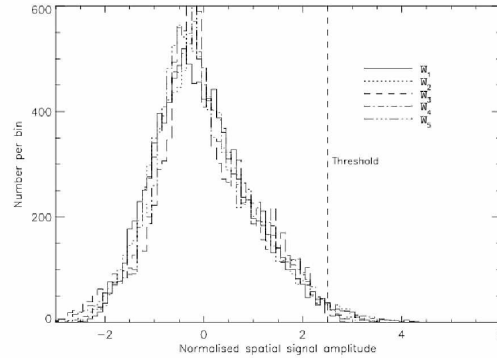


**Figure 3.** Distribution of normalised amplitudes from spatial filter. The distribution follows a Gaussian, with a high-end tail which contains cluster candidates.

In practice, one can determine  $\Lambda$  by measuring the excess number of galaxies in the search cell (see below), and so the most likely value of  $m^*$  can be sought. Matched-filters are usually used to provide redshift estimates of clusters, and each trial  $m^*$  value can be thought of as a matched-filter redshift estimate  $z_{MF}$ , using some relation between  $M^*$  and  $m^*$  (e.g. Colless 1989). The predicted magnitude of a passively-evolving  $M^*$  elliptical, from the models of Kodama & Arimoto (1997) was used here, for consistency with the CMR method, explained in §3.2. Most implementations of the MF assume some radial profile for the model cluster fixed in metric coordinates (e.g. Postman et al. 1996; Kepner et al. 1999). This then means that  $d\Omega = d\Omega(z_{MF})$ , where  $z_{MF}$  is the Matched-Filter redshift. Lobo et al. (2000) adopted the novel approach of decoupling the assumed radial profile from  $z_{MF}$ , and just used Gaussian profiles of several different widths. Here, this is taken a stage further and a fixed angular size of detect cell  $d\Omega$  was used. One simply changes the parameterisation of radial shape and cluster richness to be contained within the  $\Lambda$  coefficient, which becomes the number of cluster galaxies within a fixed angular area. We estimated this from the number of excess galaxies over the local background value. Fixing  $d\Omega$  made the  $C$  statistic operationally easier and more stable.

### 3.1.4 Simulations

In order to test the accuracy, completeness, and spurious detection rate of the cluster-finder, an extensive set of simulations was run. First, a cluster model was required. The fiducial cluster required a model for the luminosity and spatial distribution of galaxies, since these are used by the detection algorithm. The spatial profile is given by the density profile of Navarro et al. (1997), projected into 2D using the prescription of Bartelmann (1996).

The luminosity profile was taken from the same Schechter function used by the detection algorithm. This employed the  $M_T^* = -20.68$  given by the stellar population synthesis models used (Kodama et al. 1998); we adopted  $\alpha = -1.1$  (as used by Postman et al. 1996). These authors noted that varying  $\alpha$  between  $-0.6$  and  $1.6$  only alters the FWHM of the luminosity filter by  $\lesssim 15\%$  relative to the nominal  $\alpha = -1.10$ , and has a minimal effect on the detectability of cluster candidates). The normalisation of the LF is varied, and the number of galaxies brighter than  $m_3 + 2$  within an Abell radius counted to give the Abell Richness Class (ARC, Abell 1958). Clusters from ARC 0 to 3 were simulated. The cluster models were generated in physical coordinates and then transformed to

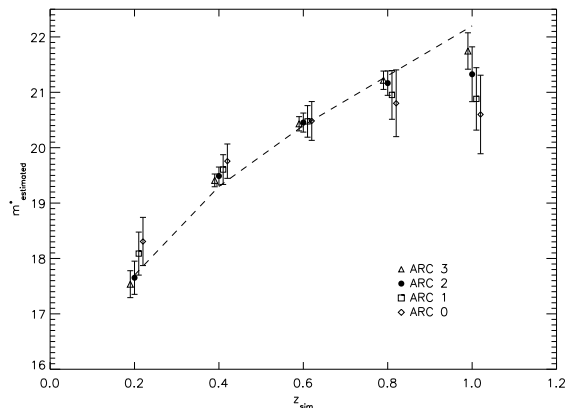


**Figure 4.** Matched-Filter Accuracy. Recovered estimate of  $m^*$  against simulated redshift. The dashed line shows the model used for the  $m^*$ - $z$  relation. Each point is the mean of 100 simulations. The points for the different richness classes are offset slightly in  $z_{sim}$ , in the plot, for clarity. Error bars are  $1\sigma$  standard deviation between all simulations.

different redshifts. For the distribution of field galaxies, points were put down randomly over the field of the WFC mosaic. Each point then had a magnitude assigned to it, extracted from the observed number counts. The number of galaxies in each realisation was allowed to vary according to the range of surface densities seen in the data.

For each richness class of cluster, 100 realisations of cluster and field were produced at each redshift interval from  $z=0.2 - 1.0$  in 0.2 steps. These mock fields were then passed to the detection algorithm. The results are plotted in Fig. 4.

The completeness was assessed from the same simulations. For every simulated cluster, the cluster was considered correctly recovered if a candidate centre lay within  $2.5W_1$  of the simulated cluster centre, and its Cash  $C$  value lay below the threshold cutoff (explained below).

To assess the number of spurious candidates detected, the algorithm was run on simulated blank fields. Other authors (e.g. Kepner et al. 1999; Postman et al. 1996; Lobo et al. 2000) have used random realisations of their data to represent blank (i.e. cluster-free) fields. However, this is likely to underestimate the false-positive rate, since the positions of galaxies on the sky are correlated. In order to account for the clustering, mock fields were generated in such a way that the positions of points obeyed the observed two-point correlation function,  $\omega(\theta)$  - a measure of the number of galaxies at a given angular separation  $\theta$  - usually modelled as a power-law in  $\theta$  (Davis & Peebles 1983). Such fields were generated using the iterative tree technique of Soneira & Peebles (1978). This was implemented using code kindly supplied by Ian Smail.  $\omega(\theta)$  is further discussed in §4.

Mock fields were generated to match the geometry of the WFC, and the MF algorithm applied. The threshold for the Cash  $C$  statistic was found by experimentation until a reasonable compromise was found between completeness and false-positive detection rate. The rates for the final threshold are plotted in Fig. 5. A value of  $C_{thresh} = -155$  in the units set out in the previous section was chosen.

To summarise, the matched-filter uses only the I-band galaxy positions and magnitudes to attempt to find systems with luminosity functions resembling those of galaxy clusters. This particular algorithm is designed to generously join points likely to belong to

a given overdensity together to allow for the possibility of irregular, extended clusters, perhaps as yet unrelaxed. The performance of this algorithm is compared with simulated data in Figs. 4 and 5. Simulated clusters of various richness classes were generated. The accuracy of the estimated redshifts is worst for the poorest clusters, but even for these it should be better than  $\Delta z=0.1$  for redshifts less than about 0.7. Hereafter the accuracy decreases, as a large fraction of the galaxies drop below the completeness limit of the survey. Again, for redshifts less than  $\sim 0.7$ , the MF algorithm should find all clusters of Abell richness classes (Fig. 5). The fraction of false detections is essentially zero below this redshift and rises (most rapidly for poorer clusters) hereafter. Thus, this algorithm should essentially recover all  $ARC>0$  clusters with negligible contamination below  $z\sim 0.7$ .

### 3.2 The Colour-Magnitude Relation Algorithm

The CMR finder used was based on the Cluster Red Sequence algorithm of Gladders & Yee (2000). Their method is directly applicable to the XDCS data set, as they tested the algorithm on V- and  $I_c$ -band data of the CNOC2 field redshift survey (Yee et al. 2000). The CNOC2 survey comprises four fields of similar area and depth to each of the XDCS fields, although the total area of XDCS is an order of magnitude larger. The algorithm works by first filtering the data, leaving only those which are compatible with galaxies belonging to a model colour slice in colour-magnitude space. Then the method proceeds in a similar manner to the previous methods - convolving the data points with a kernel and performing density estimation. However, there is now the added complication that the overdensity finding has to be done in 3D.

#### 3.2.1 Model CMRs

The passive-evolution models of Kodama & Arimoto (1997), with the cosmology  $H_0 = 64 \text{ kms}^{-1} \text{ Mpc}^{-1}$ , and  $q_0=0.1$ , and a formation redshift of  $z_f = 4.4$ , were used. These models reproduce the evolution of the CMR for clusters to  $z\geq 1$  (Kodama et al. 1998). A redshift is selected and the model colours as a function of magnitude for this redshift extracted. A colour slice of width compatible with the scatter in the CMR is taken around this line. The slices are selected in colour space and constructed in such a way that each overlaps by half the width of the next slice, in order to ensure that cluster CMRs are not lost between adjacent slices. This leads to irregular redshift spacing (e.g. Fig 6). Slices were chosen between  $V - I_c = 1.4$  and  $V - I_c = 2.7$ . Bluer than this limit and the  $4000\text{\AA}$  break passes below the limit of the V-band filter, and redder than this limit and the colour errors become unreasonably large. The model slices used are shown in Fig 6.

Each of the 24 slices illustrated is confronted with the x,y-position, colour, colour-error and total  $I_c$  magnitude data in turn. Each galaxy is then given a weight which is the likelihood that for the given V -  $I_c$ ,  $\Delta(V - I_c)$ ,  $MAG\_BEST(I_c)$ , the galaxy belongs to the model CMR slice (errors in the  $I_c$  magnitude are ignored as the CMRs are virtually horizontal). This weight shall be termed the *colour weight*. In practice, many galaxies are so far from the colour slice that their colour weights can safely be set to zero, thus galaxies with colour weights of less than 0.1 (i.e. 10 per cent probability of belonging to the CMR slice) are ignored. This is done for computational efficiency.

As mentioned above, the aim is to run kernel density estimation on the data, using colour-based weights to amplify the signal from cluster galaxies. As can be seen from the number counts,



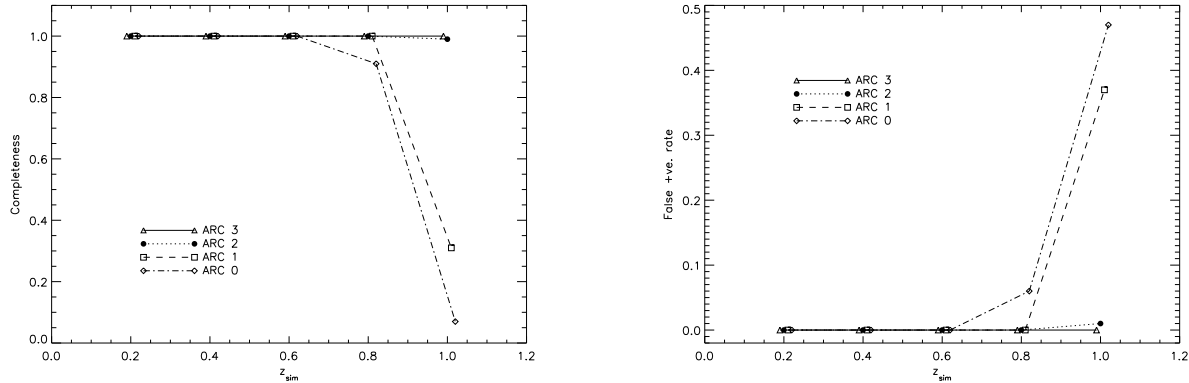


**Figure 5.** Matched-Filter Completeness (left). For the same simulations as Fig. 4, the fraction of correctly-recovered clusters (see text) was calculated. Matched-Filter Spurious Detection Rate (right). As for adjacent plot, but now the points represent detections of cluster candidates in a blank but correlated field. See text for details.

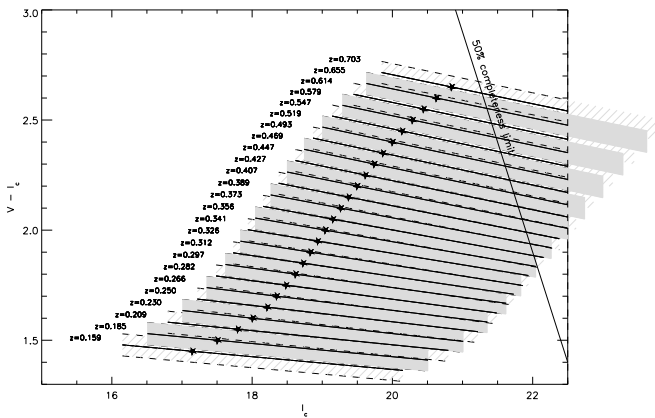


**Figure 6.** Model colour slices used in the CMR finder. Thick lines show the CMR at the redshift given to the left; stars illustrate the position of  $M^*$ ; and dashed lines show the  $1\sigma$  scatter in the CMR, bounding the slice. Colour slices run from  $M^*-1$  to  $M^*+3$  (to a limiting magnitude of  $I_c = 22.5$ ). Alternate slices are shaded differently for clarity. The 50% completeness limit of the photometry is also shown.

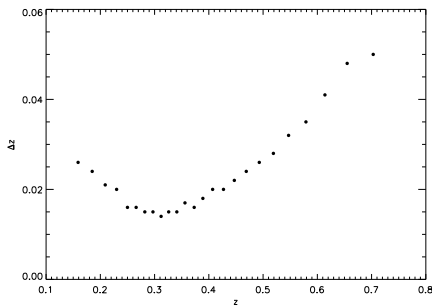


**Figure 7.** The redshift resolution of the CMR-finder. The binwidth in redshift of the model slices (spaced constantly in colour), is shown as a function of redshift. This illustrates that the method offers greatest sensitivity at  $z \sim 0.3$ , and the binwidths increase rapidly above  $z \sim 0.5$ . Also, increasing colour errors and incompleteness lead to increasing uncertainty in redshift estimation at the high end.

the numbers of galaxies at faint magnitudes grows rapidly. Thus, if just the colour weights were used, spurious detections would be caused due to some fields containing large numbers of faint objects (many of which would have the same colour as the CMR slice). Put simply, brighter (and rarer) galaxies are more powerful diagnostics of cluster members. Hence, it is necessary to also apply *magnitude weights* to weight brighter objects more heavily, within each colour slice. The form of this weighting function was determined by Gladders & Yee (2000) for the CNOC2 data. This function is the probability that a galaxy of a given magnitude is a cluster galaxy. It could be derived from theoretical models, but requires the cluster galaxy LF; the space density of clusters and its evolution; and the field galaxy counts: it is simpler to deduce internally from the data. Gladders & Yee (2000) show that whether they assume 2% or 20% of all their galaxies lie in clusters, the fit to the weighting function only differs in linear slope by a factor of 1.5 (although there is considerable scatter about the relation). Bearing this in mind, the function chosen here is a fit to the result in their Fig. 5.

$$P(M) = \begin{cases} 0.55 & (M^* - 1 < M < M^*) \\ -0.08(M - M^*) + 0.55 & (M^* < M < M^* + 3) \end{cases} \quad (7)$$

Once colour weights have been assigned, each galaxy is given a *total weight* for each colour slice which is just the product of the colour weight and the magnitude weight. The next step is to smooth the data with a kernel and estimate the density of the weighted points. In a change from the previous method, a regular grid is chosen. This makes several later stages computationally easier. A grid fixed in physical size (for the above cosmology) is constructed with the pixels spaced in intervals of  $0.125 \text{ h}^{-1} \text{ Mpc}$ . The kernel chosen also differs from the Gaussian kernel used in the above methods. Gladders & Yee (2000) chose to use an exponential kernel of the form  $k(r) = Ae^{(-1.965r)}$  where  $A$  is a normalising constant (although this is unnecessary, as a further normalisation step is carried out later in the algorithm, and so  $A$  is ignored here) and  $r$  is the physical distance between galaxies at the redshift of the colour slice, in units of  $0.33 \text{ h}^{-1} \text{ Mpc}$ . They chose this kernel as it approaches the shape of the NFW profile at intermediate radii (for the value of -1.965 chosen) and is constant provided that  $r$  is given in units of the NFW scale radius (a value of  $0.33 \text{ h}^{-1} \text{ Mpc}$  is suggested by the CNOC1 survey (Carlberg et al. 1996)).

Thus, running the above algorithm results in a series of grid points distributed over the field of view, each with an associated signal resulting from the convolution of the exponential kernel with

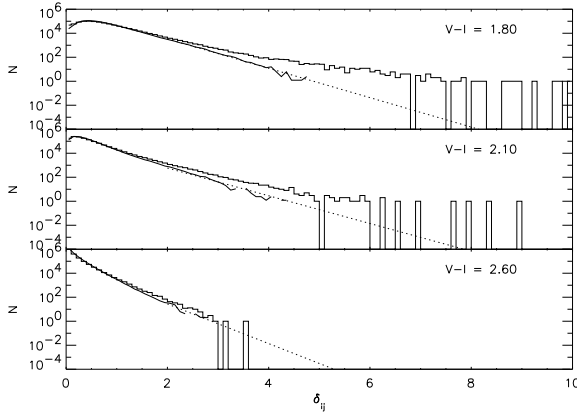


**Figure 8.** Histograms of  $\delta_{ij}$  values for CMR-finder. Three different colour slices are illustrated. The solid histogram shows the binned values for the whole survey. The thick, solid line shows the values for the bootstrapped-thresholded data, and the dotted line is the power-law extrapolation to the bootstrap. See text.

the total weights. These signal amplitudes will be referred to as  $\delta_{ij}$ s in the notation of Gladders & Yee (2000). Each colour (redshift) slice contains a different number of grid points (as the angular size of the field is fixed, but the physical scale at the redshift of the slice decreases with increasing redshift), and a different distribution of  $\delta_{ij}$ s. The distribution changes as the fixed physical size kernel changes apparent size and the mean density of objects differs between redshift slices. Thus, the  $\delta_{ij}$ s need transforming into some standard measure of significance, correctly normalised between the colour slices.

Several cluster detection algorithms (Gal et al. 2000; Lobo et al. 2000; Gladders & Yee 2000) have used bootstrap resampling techniques to assess the significance of detections, and this was also done here. As noted by Gladders & Yee (2000), a direct application of the bootstrap is likely to be incorrect (as the data contains clusters and is therefore not independently distributed). So, exclusion cuts of 10% of the data at the high- $\delta_{ij}$  and low- $\delta_{ij}$  (to preserve symmetry) ends were performed; and each data point (comprising an x,y-position, colour, colour-error, and magnitude) was sampled, with replacement, until the original number of datapoints had been extracted. The bootstrapped datapoints were then run through the algorithm, resulting in a new distribution of bootstrapped  $\delta_{ij}$ s. Each WFC mosaic had one bootstrapped realisation of its data made, as the process is computationally expensive. A power law fit of the high significance tail was extrapolated to the very rare, highest significance peaks. This was found to agree well with tests made for larger number of realisations. The high- $\delta_{ij}$  tail (where the number of points is low) can be extrapolated well with a simple linear fit, rather than performing many more bootstrap resamplings. See the distributions illustrated in Fig. 8, and cf. fig. 7 of Gladders & Yee (2000). The probability that a given  $\delta_{ij}$  occurs at random can be found by comparing the number of  $\delta_{ij}$ 's in a given range with the number in the same range in the clipped-bootstrap sample,  $P(\delta_{ij}) = \frac{N(\delta_{bootstrap} \geq \delta_{ij})}{N(\delta_{bootstrap})}$ . These can then be stated as the equivalent Gaussian sigma (denoted  $\sigma_{ij}$ ) for convenience.

The final step in this process is to extract the significant peaks, and work out which peaks are associated (i.e. part of the same cluster). The above  $\sigma_{ij}$ 's form a datacube in x,y,z space, where x,y are the physical metric coordinates

and z is the redshift of each slice. Gladders & Yee (2000) used the clump-finding algorithm `clfind` of Williams et al. (1994) to extract significant associations from the data. A user-friendly IDL version of this algorithm was downloaded from <http://www.astro.ufl.edu/~williams/clfind/> and run on the datacubes using the parameters detailed in Gladders & Yee (2000). Briefly, the algorithm is a 3D friends-of-friends group-finder which also contours the data at fixed intervals and looks for clumps in this 4D space. The code was originally used with temperature maps in radio data, but the temperature can be replaced with the signal from the CMR-finder, and the method is identical. The highest peaks are identified first and traced down in contour levels, their friends above the minimum level being linked to them at each interval. Following this through, all points become joined into one clump as the lowest contour level approaches the noise within the data. From extensive simulations, Williams et al. (1994) recommend the data be contoured at intervals of twice the *rms* noise in the data. Gladders & Yee (2000) calculated this value to be  $1.1\sigma_{ij}$ . Tests were performed varying this value. The resulting groups found were practically identical, but using a value of  $1.4\sigma_{ij}$  seemed a slightly better choice. Using a lower value split off clumps around the periphery of higher significance clumps (described in more detail below). The peaks were traced down to the lowest possible contour level ( $1.1\sigma_{ij}$ ). This level resulted in a total catalogue of  $\gtrsim 1000$  candidates. This number was reduced by setting a higher threshold later, by examining the repeatability of cluster detections in the overlapping data. A threshold of  $4.8\sigma$  was found to result in a reasonable number ( $\sim 200$ ) of repeatable candidates, detected in the two independent images. This high value may suggest that the bootstrap estimate used may be an overestimate of the formal significance of candidates. It should be noted that changing the size of the high and low exclusion cuts used in the bootstrap realisations will change the absolute values of the significances. However, since the relative significance is correct, just selecting a subsample of the most significant systems is a perfectly valid approach.

Thus a list of cluster candidates was extracted from the datacubes. One further stage was necessary to clean the resulting catalogues, as a number of candidates were found in close proximity to more significant candidates.

These may be genuine groups infalling into larger clusters, or just spurious detections from increased noise around other candidates. Failure to remove these would result in the following problem: when measuring properties (such as richness, see below) of the detected systems, if a cluster and poor group are superposed along the same line, very close together on the sky, then the effect on the richness measurement of the richer system would be minimal; but the effect on the poorer system would be to catalogue another rich system (due to contamination from the richer cluster). Hence, a minimum distance in physical and redshift space was imposed to prevent these duplicate detections, and only the highest peak within two cutoff radii (i.e. 8 times the NFW scale radius of  $0.33 h^{-1} \text{Mpc}$ ) and two redshift slices retained. An estimate of a characteristic radius for each group was made (as for the MF algorithm) by taking the maximum distance between the candidate centre and the  $3\sigma$  contour.

## 4 RICHNESS MEASURES

One of the simplest observables for a galaxy cluster, in optical data, is its richness. The original richness classification of

Abell (1958) has been shown to be subject to many biases (e.g. Lucey 1983; Katgert et al. 1996; van Haarlem et al. 1997). However, more recent estimates such as the  $B_{gc}$  parameter of Longair & Seldner (1979) correlate well with cluster velocity dispersion (e.g. Hill & Lilly 1991; Yee & López-Cruz 1999).

#### 4.0.2 The $B_{gc}$ Measure

$B_{gc}$  is explained in detail in Yee & López-Cruz (1999) and references therein. It has been used by several workers, primarily in studies of the environments of radio galaxies (for recent examples: Andersen & Owen 1994; Miller et al. 1999). In outline, it is found from the amplitude of the 3D two-point correlation function. The 3D correlation function is difficult to measure; observationally easier is the angular correlation function,  $\omega(\theta)$ . This is simply a measure of the number of galaxies at a given angular separation. This can be approximated as a power law  $\omega(\theta) = A_{gg}\theta^{1-\gamma}$  (Davis & Peebles 1983, for example), where  $A_{gg}$  is the angular galaxy-galaxy correlation amplitude. Now, fixing a reference point as the assumed centre of the cluster, one can measure the two-point angular galaxy-cluster correlation function. Its amplitude,  $A_{gc}$ , can be calculated by counting the excess number of galaxies (i.e. background-subtracted), within some radius,  $\theta$ , of the cluster centre ( $N_{net} = N_{total} - N_{bgd}$ ). Assuming fixed  $\gamma$ ,  $A_{gc} = (N_{net}/N_{bgd})[(3-\gamma)/2]\theta^{\gamma-1}$ .

$B_{gc}$ , the spatial amplitude, can be estimated via deprojection of the angular correlation function, assuming spherical symmetry, as given in Longair & Seldner (1979):

$$B_{gc} = N_{bgd} \frac{D^{\gamma-3} A_{gc}}{I_\gamma \Psi[M(m_0, z)]} \quad (8)$$

where  $N_{bgd}$  is the background galaxy counts to apparent magnitude  $m_0$  and  $\Psi[M(m_0, z)]$  is the integrated LF of galaxies up to the absolute magnitude  $M$ , given by  $m_0$  at the cluster redshift  $z$ .  $I_\gamma$  is an integration constant arising from the deprojection ( $I_\gamma = 3.78$  for an assumed  $\gamma$  of 1.77).  $D$  is the angular diameter distance to  $z$  (Equation 1).

Yee & López-Cruz (1999) discuss extensively the effects of different assumptions/ measurement limits on  $B_{gc}$ . The salient points are summarised here. If the assumption of a universal LF is not strictly correct, then the systematic uncertainty this introduces in  $B_{gc}$  is  $\sim 10\%$ . Changing the parameters of the LF (slope and normalisation) results in  $\lesssim 20\%$  differences in  $B_{gc}$  if  $M^*$  is incorrect by as much as 0.5 mags, and if  $\alpha$  is incorrect by as much as  $\pm 0.3$ .  $B_{gc}$  is independent of the sampling area, provided  $\gamma$  has been correctly chosen.  $B_{gc}$  is insensitive to the sampling magnitude limit if  $m_{lim}$  lies on the flat part of the LF (between  $M^*+1$  and  $M^*+2$ ). The most important step is ensuring that the cluster LF and background galaxy counts are determined in a self-consistent manner.

The model LF is the same as that chosen for the cluster in the MF algorithm. Fig. 2 illustrates how the model LF assumed for both the cluster and the field translates into field galaxy counts. The LF was integrated over 0.05 redshift bins from  $z = 0.00$  to  $z = 2.00$ .

The normalisation,  $\phi^*$ , was fitted to the XDCS data.  $\phi^* = 0.0035 h_{64}^3 \text{Mpc}^{-3}$  was found. This is consistent with the R-band value measured by Yee & López-Cruz (1999), after correcting the number density to their cosmology. The completeness was modelled as XDCS counts/ literature counts (from Metcalfe et al. 2001) to  $I_{lim} = 22.5$  (where the completeness falls to 70%). This factor was then applied to the expected counts for the  $B_{gc}$  calculation (as well as to the MF algorithm, earlier).

The uncertainty in the  $B_{gc}$  parameter was computed using the formula from Yee & López-Cruz (1999):

$$\frac{\Delta B_{gc}}{B_{gc}} = \frac{(N_{net} + 1.3^2 N_{bgd})^{1/2}}{N_{net}} \quad (9)$$

The factor  $1.3^2$  accounts for the clustered (and so non-Poissonian) nature of the background counts (Yee & Green 1987).

#### 4.0.3 The $L_E$ Measure

The luminosity of galaxies on the CMR referred to as  $L_E$  (since the galaxies are primarily early-type), has been shown (for a limited sample) to correlate well with the X-ray temperature of the cluster (Smail et al. 1998). For a sample of the 10 most X-ray luminous clusters in the redshift range  $z = 0.22 - 0.28$ , Smail et al. (1998) investigated the homogeneity of the stellar populations of cluster early-type galaxies. One method they used was to compare mass of baryonic material locked up in stars in early-types (in the form of the luminosity of galaxies on the CMR) with the total mass of the cluster (using X-ray temperatures from the literature). They found a remarkably small scatter about this relation ( $\approx 17\%$  compared to the  $\approx 30\%$  when  $L_X$  is used instead of  $T_X$ ). It should be noted that the sample spans a narrow range in redshift, and relatively narrow range in blue fraction (i.e. few galaxies statistically belonging to the cluster are *not* red), and mass. A large sample to characterise an empirical relation between  $L_E$  and  $T_X$  (or mass) over a larger range of parameter space does not currently exist in the literature. However, the evolution of cluster mass-to-light ratios for a sample of 4 X-ray selected clusters over a wide range ( $0.22 < z < 0.83$ ) of redshift has been studied by Hoekstra et al. (2002). Using gravitational weak-shear measurements from HST images, they determined that the mass-to-light ratios in their sample evolve in a manner consistent purely with luminosity-evolution of the cluster early-type galaxies. Thus, inverting this argument, measuring the rest-frame luminosity of cluster early-type galaxies (corrected for passive evolution) could potentially provide an estimate of the total cluster mass. Again it should be emphasized that the datasets on which these correlations were based are small and so the scatter in the relation is not well known. Furthermore, all the data came from X-ray selected samples, so the scatter may be further increased once optically selected clusters are included.

For each cluster candidate, the colour slice from the CMR-finder in which the candidate was detected was selected. The galaxies within this colour slice, and within a radius of 0.45 Mpc (0.5 Mpc in Smail et al. 1998 cosmology) brighter than  $M_V = -18.5 + 5 \log h$  (Smail et al. 1998) were selected, and their apparent I-band magnitudes converted into rest-frame V luminosity, again using the stellar population synthesis models of Kodama & Arimoto (1997). This magnitude limit is approximately 1.5 magnitudes fainter than  $L^*$  at  $z \sim 0.3$ . Background subtraction was carried out by calculating the number of galaxies in a surrounding annulus, scaled to the area of the cluster region, as above, and subtracting the corresponding luminosity, assuming these galaxies were at the same redshift as the cluster. The limits for the maximum and minimum luminosity were estimated by using all the galaxies whose photometric colour errors allowed them into or out of the colour slice, respectively, and summing their luminosities in the same way. This gives error estimates in excellent agreement with assuming the error is entirely due to the error in the estimated redshift (by taking the redshifts of the next highest and lowest colour slices and recalculating the luminosities).

#### 4.1 Construction of Final Cluster Catalogues

Both the MF and CMR finders were run on each WFC mosaic individually. Since each field possesses overlapping ‘A’ and ‘B’ data, the next step is to combine the candidates from the A- and B-rotations, for each algorithm. The MF technique is more straightforward, so this will be discussed first.

The MF catalogue was divided into two catalogues with different significance thresholds. The higher significance catalogue will be referred to simply as the MF catalogue, or the *final* MF catalogue, if it is necessary to emphasize the distinction between this and the lower-significance catalogue: referred to as the *full* MF catalogue. The full MF is that using the thresholding described in §3.1.4. The final MF catalogue was produced by imposing a stricter Cash  $C$  cut (a value of  $-280$ , this time). The completeness and spurious rates with this threshold are comparable to those plotted in Fig. 5 for redshifts less than 0.7. Using higher redshift candidates just increases the number of spurious detections, and the X-ray data are unlikely to probe enough volume to detect clusters at these redshifts. Also, candidates with a MF group radius of zero were rejected. Such objects occur when only a single galaxy (and none of its near neighbours) lies above the Cash  $C$  threshold. This reduces the number of clusters detected to a more manageable number,  $\lesssim 200$ , of higher confidence candidates, whilst the full MF catalogue allows the list of lower significance candidates to still be retained. This may prove useful later, if, for example in cross-comparisons between catalogues, a candidate is not found with high significance in the MF catalogue; then the full MF catalogue may be searched.

Next, I-band WFC thumbnail images were produced for all candidates in the MF catalogue. These were inspected to see if a candidate was found due to spurious objects (e.g. satellite trails, haloes of bright stars). Those that were spurious were flagged and rejected from the catalogue. Finally, the MF catalogue comprising A- and B-rotation candidates was reduced to a single catalogue by searching for candidates which overlapped in the two rotations. Where this occurred, only the candidate with the larger group radius was retained. This was found to be more stable than selecting the highest peak Cash  $C$  value candidate, as the group radius is given by the extent of galaxies passing the Cash  $C$  cut; but the Cash  $C$  value noted for each candidate just comes from the galaxy with the highest individual value in the candidate. This can be thought of as favouring a larger “total likelihood” over that of a “peak likelihood” for each cluster candidate.

The procedure for producing the CMR catalogue was slightly more involved. This was due to the ‘3D’ aspect of finding clusters with this technique. Whereas the MF finder just selects overdensities and fits the most likely redshift to the clump, the CMR finder can, in principle, detect projections of groups along the line of sight. The same first steps as for the MF were followed: I-band thumbnails were generated, spurious candidates rejected, and a higher and lower significance catalogue generated. The final CMR catalogue had a threshold of  $4.8\sigma$  imposed, as described in §3.2, whereas the full (lower significance) catalogue allowed candidates to be traced down to the lowest possible contour level with `clumpfind` (i.e.  $1.4\sigma$ ). Candidates in the *same* rotation which showed more than one candidate overlapping (as defined by their group radii) were flagged as ‘projection’ possibilities. This check was performed on an individual frame basis to avoid the possibility that a single candidate having a significantly different estimated redshift in the A- and B-rotations would result in one candidate

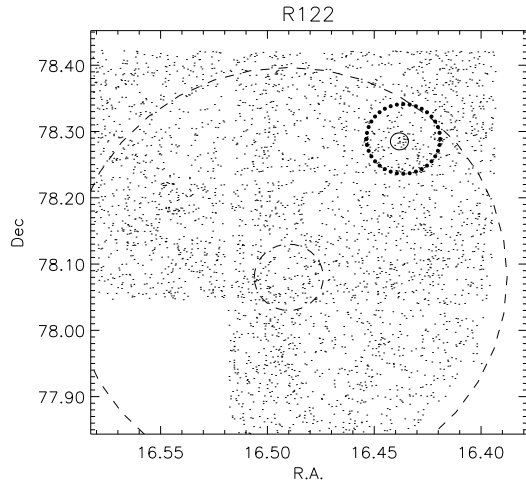


**Figure 10.** Final catalogues for this field. The thresholding described in the text has been applied. Dotted circle denotes MF candidate, solid line shows CMR candidate. Other symbols as for previous figure.

being artificially classed as a projected system. The final CMR catalogue was produced by combining the rotations as for the MF.

This provided the two main catalogues for the optical survey: the final MF catalogue and final CMR catalogue. These catalogues were then passed to the richness measuring algorithms described in 4. Finally, both catalogues were cropped to overlap with the X-ray data which is described below. To do this, only candidates within an annulus of 3 to 19 arcmins from the centre of the X-ray pointing were retained. At distances greater than this, the X-ray data are not useful (due to degraded resolution and sensitivity - see below) and the inner region was excised to avoid objects associated with the target of the X-ray observation.

##### 4.1.1 Summary of Catalogues

In total, the final MF catalogue (constructed and trimmed to the PSPC field, as described above) contains 185 cluster candidates. The final CMR catalogue contains 290 candidates. The MF technique fits the most likely value of  $M^*$  in the range  $17.0 \leq I_C \leq 21.5$ . The bright limit is imposed by there being few galaxies this bright in the field, and at this redshift ( $z=0.15$ ) the angular diameter of clusters becomes so large that the contrast of the cluster against the background is greatly reduced. The faint limit (corresponding to  $z=0.9$ ) is set such that the limiting magnitude is one magnitude fainter than this  $M^*$ , thus there are still many galaxies to which to fit a luminosity function. The CMR method is limited by the depth of the photometry in *both* bands (as illustrated in Fig. 6), which leads to colour limits  $1.45 \leq V-I \leq 2.65$  corresponding to  $0.159 \leq z_{est} \leq 0.703$ . In practice, the MF catalogue is cropped at the high redshift end to match the colour limits imposed by our choice of filters used with the CMR method. At the low redshift end, only a few clusters lower than the our CMR colour limit are found by the MF, so these are retained.

#### 4.2 Internal Check of Redshift Estimates

To assess the accuracy with which an estimated redshift can be assigned, an internal check can be performed comparing the redshifts estimated for candidates using the A- versus the B-rotation data.

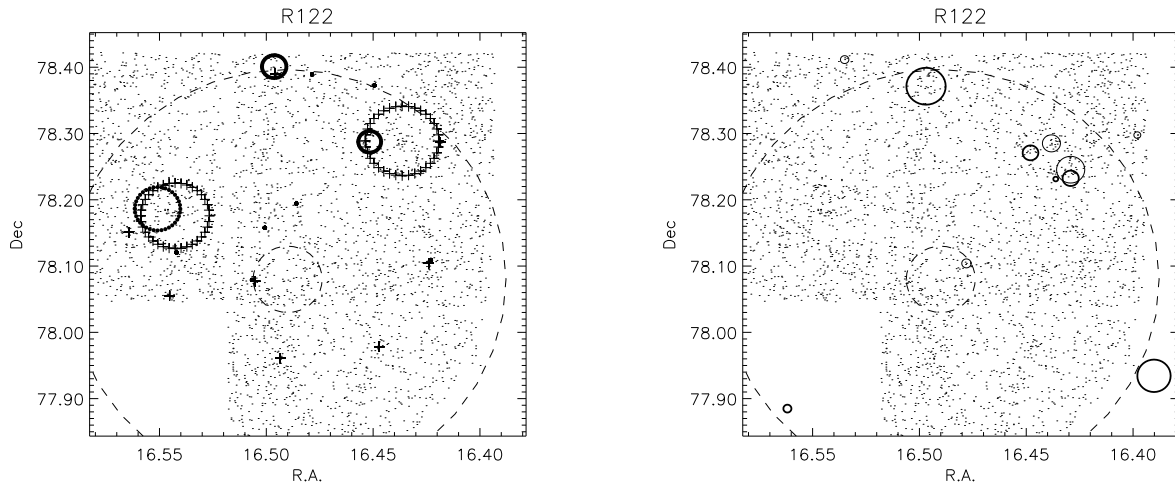


**Figure 9.** Full catalogues in one field for MF (left) and CMR (right) algorithms. Points show galaxies with I-band magnitudes brighter than 22.5 (for B-rotation only, for clarity). Dashed lines denote the limits of the PSPC field (19 arcmins: outer radius, 3 arcmins: inner radius). Cluster candidates are outlined by points marking their group radii (defined in text). Symbols are:

Left panel, MF candidates: filled circles - A-rotation; crosses - B-rotation.

Right panel, CMR candidates: thick lines - A-rotation; thin lines - B-rotation.

Those candidates which appear as single points have group radii of zero (see text).

Due to the way in which the object catalogues are generated (§2.2), different data are produced for the same region of sky using two independent observations. For example, the main difference between object catalogues for the two rotations was the star/ galaxy classification. Several objects classified as galaxies in one rotation were classified as stars in the other, and vice versa. The neural network classifier of SEXTRACTOR uses both the FWHM of a source and its ellipticity to decide the nature of each source. The effect of FWHM differences was minimised due to the way in which the data were taken (observing the same A- and B-rotation fields sequentially) so that, unless the seeing is changing on very short timescales, the FWHM of point sources should be the same for the two rotations. Inspection of objects which changed class between the two frames showed that a slightly different measure of ellipticity was the primary cause. Overall, the level of star/ galaxy misclassification should be around the few percent level. From the spectroscopic observations presented in §7, two of the 87 redshifts measured (for objects brighter than  $I \approx 20$ , classified as galaxies) were due to stars, or around 2%. The contamination is likely to be higher for fainter objects, where a lower signal makes shape parameters more difficult to measure. To a lesser extent, the object catalogues between the two rotations differ due to cosmic rays, diffraction spikes, and differently deblended objects (as discussed in §2.2).

A comparison of estimated redshifts between the two independent observations allows the effect of all these factors to be taken into account. This is one of the primary motivations for treating the repeat observations separately. Candidates for the comparison were selected in the following manner. For the MF catalogue, the full catalogue was compared with the final catalogue. For each entry in the final catalogue, if a single candidate from each rotation was present in the full catalogue, within the final catalogue entry’s group radius (to avoid possible confusion with multiple matches), then the candidate was selected. A similar procedure was followed for the CMR catalogue, with the added condition that the candidate must not be flagged as comprising projected groups (again to avoid confusion due to multiple matches). In both cases a limiting radius of 1 arcmin was imposed for the match, to ensure a high level of confidence that

the same candidate had been selected from the two datasets. The comparison of the estimated redshifts from each rotation for each cluster detection algorithm is shown in Fig. 11. Quantifying the bias and scatter in these relationships as:  $\delta z = (z_A - z_B)/(1 + z_A)$  (e.g. Wittman et al. 2001), the mean value is -0.004 for the MF and -0.014 for the CMR algorithm; the standard deviations are 0.097 and 0.081 respectively. This is somewhat misleading as the majority of the scatter from the CMR comes from a few outliers, and the majority of points show excellent agreement between the two independent observations. A large fraction of the outliers were detected in the final ( $z=0.70$ ) colour slice in one rotation, and thus could easily be missed and associated with a less significant lower redshift clump in the corresponding rotation. The few other outliers can be understood in terms of marginal cases for projected systems. If each rotation detects two systems, the lower significance candidate is measured as being more significant in the overlapping rotation, and the lowest significance system falls below the threshold in both cases, then a catastrophic failure of the redshift estimate would occur. This only appears to be the case for seven of the systems in the plot, at  $z_{est} < 0.69$ . The scatter in the MF estimate is intrinsically large. Neither estimate shows any significant bias between the two datasets.

## 5 X-RAY SELECTION OF CLUSTERS

The X-ray data are archival images taken with the ROSAT Position Sensitive Proportional Counter (PSPC). Such observations are divided into two energy bands: “hard” (0.4–2.4 keV) and “soft” (0.07–0.4 keV). The background flux is particularly high at energies below 0.5 keV and the sensitivity of ROSAT rapidly drops to zero above 2.0 keV. As a result, most X-ray cluster surveys use the hard band and cut its range down to 0.5–2.0 keV. All of the fields were taken from the RIXOS survey (Mason et al. 2000), which was an international campaign to follow up in the optical all X-ray sources in a sample of ROSAT PSPC fields above a point source flux limit of  $3 \times 10^{-14}$  erg cm<sup>-2</sup> s<sup>-1</sup> (0.5–2.0 keV). Thus,

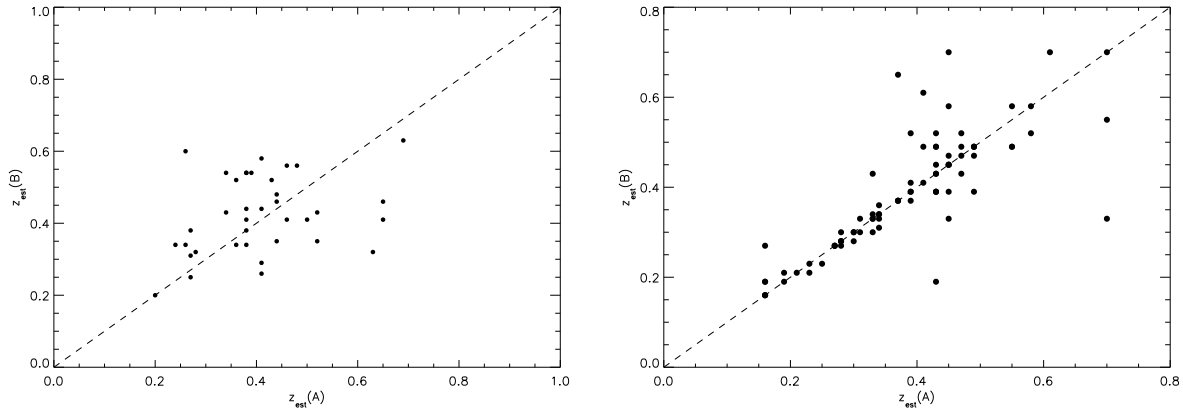


**Figure 11.** Comparison of estimated redshifts for the MF and CMR algorithms from the A versus B data. The left panel shows the MF estimated redshift in the B field versus the A field estimate of the same quantity. The right panel shows the A versus B estimated redshift for the CMR algorithm.

a sample of clusters discovered in the X-ray in these fields have already been selected and confirmed. However, the algorithm with which these were found was optimised for point source detection, and not for locating extended emission, as expected for clusters of galaxies. Thus the RIXOS cluster catalogue is incomplete. This resulted in a claim for a deficit of high redshift clusters in the RIXOS sample (Castander et al. 1995), when other investigators found no evolution in the abundance of clusters (e.g. Nichol et al. 1997).

The currently favoured technique for the detection of faint, extended sources in X-ray data is the wavelet method. Sources are detected by convolving the data with a kernel to enhance the contrast between objects and the background, in the same way as described in §3.1.2 for the optical algorithms. The difference with the wavelet method is that this kernel consists of a positive core and a negative outer ring (such that its integral over the x,y plane is zero). This means that slowly varying backgrounds which can be approximated by linear functions are completely subtracted. Furthermore, a wavelet transform of the data reveals sources bounded by a ring of zero values; the diameter of the zero-rings gives a measure of the angular extent of the source. In practice, a range of kernel values is used (as was done with the Gaussian filtering of the MF method), and these can be used to infer the source radius. An instructive illustration of this technique is given in fig. 2 of Vikhlinin et al. (1998).

Given that several wide-field surveys have also made use of archival ROSAT data for the serendipitous discovery of clusters (e.g. Jones et al. 1998; Romer et al. 2000; Vikhlinin et al. 1998), it is natural to check if any of these overlap with the fields selected for XDCS. 29 out of the 39 fields were used in the 160 square degree survey of Vikhlinin et al. (1998). This catalogue has the attractive feature that nearly all of the 200+ sources detected have been followed up in the optical, many possessing spectroscopic confirmation. Furthermore, their spurious detections are also recorded in their paper, so *all* X-ray detected cluster candidates can be examined, and not just the optically confirmed ones. 19 likely false detections, arising from concentrations of point sources, were recorded, but none of these occurs in the XDCS fields. Of the remaining 10 fields, 7 were included in the Bright SHARC Survey (Romer et al. 2000). Both of these used wavelet detection algorithms in their construction. The SHARC catalogue has had a fairly bright ROSAT count-rate limit imposed (corresponding to a flux of approximately  $10^{-13}$  erg s $^{-1}$  cm $^{-2}$ , or about an order of magnitude brighter than typical XDCS field limits) in order to reduce

the numbers of clusters found, to make optical follow up achievable in a reasonable amount of time. Given this limit, 94 sources were found in 460 ROSAT fields. It is not too surprising, then, that in the seven fields overlapping with XDCS, no sources are found. The SHARC survey is not considered hereafter. The Vikhlinin et al. (1998) catalogue (VMF), on the other hand, contains 15 X-ray selected clusters in XDCS fields. This is the X-ray selected cluster survey with which the XDCS optical catalogues will be compared.

The ROSAT fields observed are given in Table 1. The VMF clusters in common fields are given in Table 2.

## 6 COMPARISON OF OPTICAL AND X-RAY SELECTED CLUSTERS

The VMF X-ray selected clusters are listed in Table 2. Vikhlinin et al. (1998) used several methods to “confirm” their X-ray cluster candidates and it is pertinent to comment on these here. Aside from the traditional method of requiring an overdensity of galaxies in the optical, they included another possible criterion which was that if an elliptical galaxy not included in the NGC catalogue lay at the peak of the X-ray emission then this should be considered confirmation.

This latter point was designed to include “poor clusters and groups which fail to produce a significant excess of galaxies over the background”. The authors state that it also helps to identify “fossil groups” in which galaxies have merged to form a single cD (Ponman et al. 1994; Jones et al. 2000). Such systems appear to be as X-ray luminous as other bright groups or poor clusters, but with a high percentage of the optical luminosity arising from the dominant giant elliptical. The second brightest group member is a factor of 10 fainter than the brightest (resulting in a gap of 2.5 magnitudes in the LF). Recent work estimates that such systems comprise 8–20% of all systems of the same X-ray luminosity (Jones et al. 2003).

Vikhlinin et al. (priv. comm.) obtained optical follow up either from second generation Digitized Sky Survey (DSS-II) plates, or R-band (or sometimes B-, V-, or I-) CCD imaging on 1m class telescopes. Long-slit spectroscopy was also obtained for some candidates, usually for 2 - 3 galaxies per cluster, and always including the brightest galaxy.

To quantitatively compare the optically selected catalogues with the X-ray selected clusters, the following method was used. For each of the final MF and CMR catalogues, cross-correlation

**Table 2.** VMF clusters in XDCS fields. Redshifts are given for all but one cluster. The type of redshift measured by VMF is given in the final column (p - photometric, s - spectroscopic)

VMF ID	RIXOS Field	$\alpha$ (J2000) [hh:mm:ss.s]	$\delta$ (J2000) [dd:mm:ss]	$F_X$ $10^{-14}$ erg s $^{-1}$ cm $^{-2}$	$\delta F_X$ $10^{-14}$ erg s $^{-1}$	z	Redshift Type
11	R262	01:24:35.1	+04:00:49	7.5	2.2	0.27	p
62	R221	08:49:11.1	+37:31:25	14.7	3.0	0.240	s
69	R248	09:10:39.7	+42:48:41	8.3	2.0	—	—
73	R285	09:43:32.2	+16:40:02	23.1	3.7	0.256	s
74	R285	09:43:44.7	+16:44:20	21.2	4.1	0.180	s
84	R231	10:10:14.7	+54:30:18	21.0	2.9	0.045	s
86	R231	10:11:26.0	+54:50:08	20.0	5.1	0.294	s
94	R133	10:56:12.6	+49:33:11	12.9	1.9	0.199	s
97	R258	11:17:26.1	+07:43:35	6.1	1.6	0.40	p
99	R123	11:19:43.5	+21:26:44	5.5	0.9	0.11	p
131	R265	13:09:55.6	+32:22:31	9.0	2.9	0.290	s
132	R265	13:11:12.8	+32:28:58	46.7	5.8	0.245	s
150	R254	13:43:29.0	+55:47:17	17.5	2.8	0.11	p
181	R223	16:33:40.0	+57:14:37	3.5	0.7	0.239	s
194	R220	17:29:01.9	+74:40:46	17.3	7.2	0.28	p

**Table 3.** The nearest optically selected candidates to the VMF clusters. For each X-ray selected cluster, the nearest matching MF and CMR candidates' details are given. Candidates in parentheses were not identified in the final catalogues. See text for details.

- \* - candidate matched at a separation greater than its estimated radius.
- \*\* - candidate matched within its estimated radius, but greater than 2 arcmins.
- (p) - candidate flagged as exhibiting projection along line-of-sight.

VMF ID	MF candidate ID	$z_{VMF}$	Separation (arcmin)	$z_{MF}$	$\Delta z$	CMR candidate ID	offset (arcmin)	$z_{CMR}$	$\Delta z$
11	(mfJ012435.6+040107)	0.270	(0.328)	(0.422)	0.152	cmJ012437.8+040022	0.807	0.360	0.090
62	mfJ084914.5+373123	0.240	0.678	0.276	0.036	cmJ084908.8+373036	0.939	0.190	0.050
69	mfJ091049.4+425002	—	(2.246**)	0.484	—	cmJ091045.1+424955	1.596	0.450	—
73	mfJ094350.5+164034	0.256	(4.421*)	0.351	0.095	cmJ094329.3+163916	1.035	0.190	0.066
74	(mfJ094344.0+164500)	0.180	(0.691)	(0.293)	(0.113)	—	—	—	—
84	—	0.045	—	—	—	—	—	—	—
86	mfJ101137.3+545036	0.294	1.698	0.276	0.018	cmJ101134.1+545014 (p)	1.168	0.330	0.036
94	mfJ105617.5+493237	0.199	0.972	0.157	0.042	—	—	—	—
97	mfJ111726.2+074316	0.400	0.306	0.232	0.168	cmJ111726.2+074319	0.258	0.370	0.030
99	—	0.110	—	—	—	—	—	—	—
131	mfJ131001.9+322110	0.290	(1.889*)	0.437	0.147	cmJ130954.0+322137	0.949	0.270	0.020
132	(mfJ131113.2+322843)	0.245	(0.259)	(0.422)	(0.177)	cmJ131111.0+322825(p)	0.664	0.210	0.035
150	—	0.110	—	—	—	—	—	—	—
181	mfJ163334.2+571457	0.239	0.853	0.395	0.156	(cmJ163337.8+571328)	1.179	(0.210)	(0.029)
194	mfJ172845.5+743945	0.280	1.487	0.484	0.204	(cmJ172946.3+744238)	3.474	(0.190)	(0.090)

with the Vikhlinin et al. (1998) catalogue was performed, retaining the nearest match to each X-ray cluster. If the X-ray cluster lay within the optical candidate's group radius, it was considered matched (the only caveat is that a minimum radius of 1 arcmin and a maximum of 2 arcmin was adopted, to ignore excessively large or small group radii, and also account for the uncertainty in the X-ray position). These matches are tabulated in Table 3. For the X-ray clusters with no matches from this process, the full catalogues for each algorithm were checked, to see if a lower significance candidate is matched. Such matches are indicated in the table by parentheses. All matches were then inspected visually and special cases are commented on. Typical data are shown in Figs 12 & 13.

## 6.1 Summary of Optical Candidates Associated with X-ray Clusters

In terms of gross numbers with this simplistic matching, the final MF catalogue contains counterparts to 7 of the 15 X-ray selected clusters, and the final CMR catalogue contains 8 of the 10 in the redshift range probed by the algorithm.

In the MF catalogue: VMF11 is not matched in the final catalogue, but is matched in the full catalogue (just below the Cash  $C$  threshold). VMF69 and 73 were both further than 2 arcmins away from the nearest candidates, but lay within the candidates' group radii. Thus, these were treated cautiously, but visual inspection showed large overdensities extending this far and thus the association of these objects seems valid. VMF74 and VMF132 were detected in the full catalogue, but did not make the higher significance cut of the final catalogue. VMF84 was undetected as its redshift is too low (0.045). VMF99 and 150 were also undetected. These fields

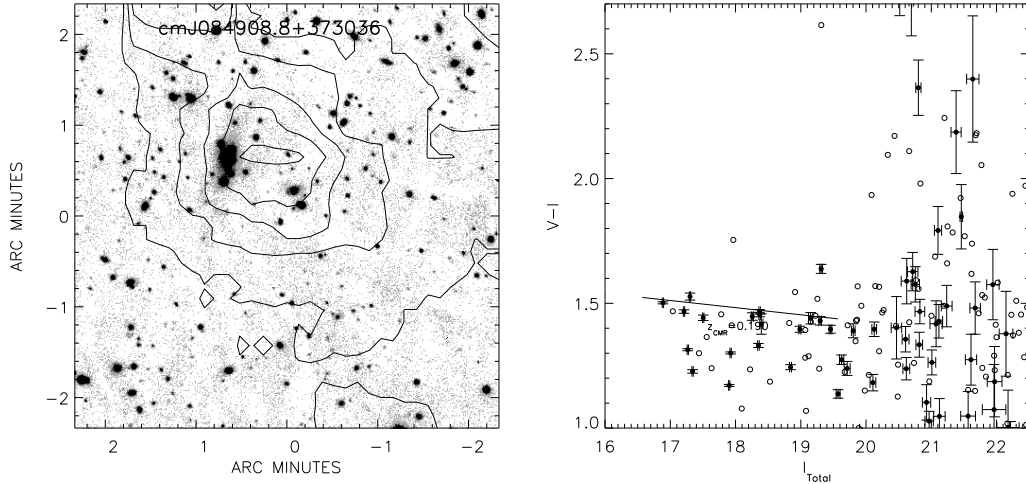


**Figure 12.** VMF62. Left panel: WFC I-band image with PSC contours overlaid (images are 5 arcmin on a side and PSC contours have been smoothed to 30 arcsec - the approximate PSF. These contours do not correspond to any particular significance level, and are simply in units of X-ray count rate). Right panel: CMD centred on VMF position. Filled circles show galaxies drawn from within 1 arcmin radius of the CMR selected candidate position; open symbols show galaxies drawn from an equal area, a further arcmin away. Note: these fixed angular radii are just chosen as a guide, and are not the same as the radii chosen by the CMR algorithm (which is colour dependant). Photometric error bars are only shown for filled points for clarity. Overplotted line shows CMR corresponding to CMR algorithm's estimated redshift (from  $M^* - 1$  to  $M^* + 2$ ). VMF62 is found in both the final MF and CMR catalogues. The associated MF and CMR candidates are listed in Table 3.

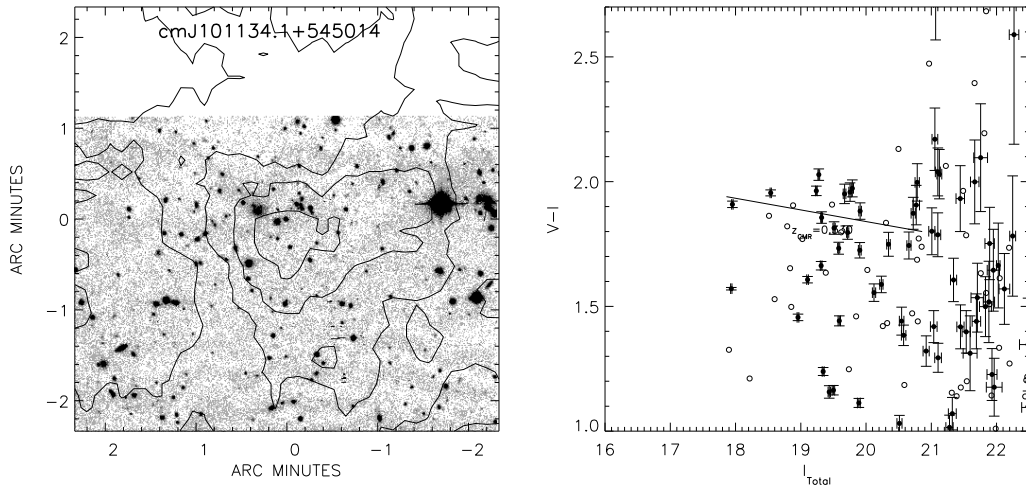


**Figure 13.** VMF86. Panels as for Fig. 12.

VMF86 appears to show a second overdensity even in the DSS image, and possibly a weak second X-ray source, although this was undetected by Vikhlinin et al. (1998) (A. Vikhlinin, priv. comm.). The second cluster centre is just visible on the extreme right of the I-band image (at  $\approx [-2.4, 0.0]$  arcmin offset). The CMD shows the hint of a second CMR 0.4 magnitudes blueward of the main candidate, mainly indicated by open symbols due to its distance from the primary candidate. Thus, this appears to be, in fact, two distinct systems at very different redshifts. Indeed, this system was flagged by the CMR algorithm as being a system suffering from projection effects.



do not show overdensities of galaxies, and the clusters were possibly ‘confirmed’ using the single luminous elliptical criterion. The redshifts given are also below the expected detection range (both have  $z=0.11$ ). VMF131 has a match at a distance of 1.9 arcmins: this is outside the candidate’s estimated radius of 0.5 arcmins, but again visual inspection suggests the association is valid. To summarise, if the three lowest redshift X-ray clusters (VMF84, 99, and 150) are excluded ( $z \leq 0.11$ ), then the strict automated matching matches 6 of the 12 candidates. Visual matching suggests the recovery rate in the final MF catalogue should be 9/12. Lowering the significance threshold allows the remaining X-ray clusters to *all* be detected (at the expense of a higher spurious rate).

In the CMR catalogue: considering all except the 5 X-ray clusters at  $z \leq 0.2$  (for the reasons described above), only two are not immediately matched. VMF181 is matched in the full catalogue and is of high enough significance ( $>6\sigma$ ) to be in the final catalogue, but was ‘cleaned’ from the catalogue as it had a neighbour of higher significance. VMF194 shows a counterpart some distance ( $\approx 3.5$  arcmin) from the X-ray cluster, but the X-ray position appears to be at least an arc minute from a significant overdensity and CMR (the MF candidate at this position was only matched because it has a large associated radius). This cluster has been the subject of extensive follow-up work by Vikhlinin and collaborators (A. Vikhlinin, priv. comm.) and was difficult to confirm optically. It has very extended X-ray emission ( $\sim 2$ -3 arcmin) and the galaxy overdensity is similarly extended. Spectroscopic follow-up found 4 out of 5 ellipticals in this field at  $z=0.213$ , and so they consider the cluster confirmed. Note that this redshift is in much better agreement with our CMR-estimated redshift than the initial photometric estimate of Vikhlinin et al. (1998).

The CMR technique, furthermore, allows the possibility of distinguishing groups projected along the line of sight (the entries in Table 3 flagged with a ‘p’). VMF86 is identified as two systems (as suspected from the data, illustrated in Fig. 13): the more significant at a redshift of 0.330 and another at 0.230. The quoted spectroscopic redshift of VMF is 0.294; this is within  $\Delta z=0.05$  of the most significant candidate. VMF132 also shows two possible further groups, overlapping with the  $z_{CMR}=0.21$  cluster, at higher redshift:  $z_{CMR}=0.37$  and 0.65. Thus, to summarise, the CMR matches 8 of the 10  $z > 0.20$  X-ray clusters immediately, and visual matching allows all 10 clusters to be matched. Another advantage of this method is that it is able to disentangle projection effects: correctly resolving structure (which is obvious visually in the CCD images) in one field, and suggesting higher redshift groups in another.

### 6.1.1 Comparison of Estimated Redshifts with VMF Redshifts

The average bias in the redshift estimate, defined as  $(z_{spec} - z_{phot})/(1 + z_{spec})$ , is 0.067 with a standard deviation of 0.066 for the MF (using 8 spectroscopic redshifts from VMF); the average bias for the CMR technique is -0.022 with a standard deviation of 0.028 (from 6 published VMF spectroscopic redshifts). The latter result compares very favourably with photometric redshifts. Wittman et al. (2001) find an average bias of -0.027 with standard deviation of 0.059 for photometric redshifts over a similar range using *four* photometric passbands. Gladders & Yee (2000) commented that redshift determination should include a step to renormalise the stellar population models to the data with redshifts. This corrects systematic offsets such as mismatches between the model and real filters. Any remaining ‘bias’ would be due to photometric calibration errors, assuming universality of the CMR.

## 6.2 Comparison of MF Catalogue with CMR Catalogue

Now that both optical techniques have been compared with a spectroscopic sample, it can be seen that the estimated redshifts from the CMR technique offer greater precision than the MF estimated redshifts. Thus, a cross-comparison of the two techniques can be made, using the CMR catalogue as a reference. The final MF catalogue was cross-correlated with the final CMR catalogue to determine cluster candidates in common. To avoid possible confusion from multiple associations of candidates, only MF candidates with a *single* CMR candidate within the former’s radius were considered. If the candidates’ centres were separated by more than two arc minutes, they were excluded. Thus, only secure ‘clean’ matches are considered. Of the 185 final MF candidates, 62 show unique CMR matches (7 of these are flagged as line of sight group projections). A comparison between the estimated redshifts of these techniques is shown in Fig. 15. The average bias and scatter (as defined earlier) in this relation are -0.066 and 0.106 respectively, although inspection shows that this may equally be due to the MF redshift being randomly drawn from values between 0.3 and 0.5. This may be due to bias in the candidates selected for this comparison (those with ‘clean’ matches between the CMR and MF candidates). A comparison of the MF estimated redshifts with those of spectroscopically determined redshifts (from the X-ray selected clusters in the next section) shows that the MF estimated redshift is not as bad as this.

A further comparison is to consider the MF candidates *not* matched with CMR candidates. This was done by comparing the full CMR catalogue with the final MF catalogue and searching for MF candidates with *no* CMR matches within their radii (or 2 arcmins). 41 of the final MF candidates show no CMR counterparts at any significance level. Under the assumption that *all* genuine clusters possess a CMR and that this technique will find them, this can be used as an approximation to the number of spurious MF detections. This gives a false detection rate of around 22%. This is in general agreement with estimates for other MF techniques of around 30% (e.g. Holden et al. 1999). 22% is a lower limit, as some of the CMR matches are of low significance. Assuming a spurious CMR rate of around 5–10% (as seems more likely, e.g. Gladders & Yee 2000; Gilbank 2001) would bring the false positive rate of the MF into closer agreement with the 30% value. Using the fraction of matched candidates flagged as projections (7 out of 62, above) compares well with the (spectroscopic) findings of Katgert et al. (1996) that around 10% of Abell clusters comprise two or more significant clusters, projected along the line of sight.

## 6.3 Comparison of Optical Richness Measures with $L_X$

Henceforth we consider only the catalogue generated by the CMR technique. We have just shown through comparison with the spectroscopically confirmed sample of Vikhlinin et al. (1998) and from internal comparisons within our data the superiority in terms of accuracy and reliability of the CMR algorithm over the MF approach.

The following procedure was used to measure the X-ray flux for each optical cluster candidate.

The relationship between each of the richness measures and X-ray luminosity for cluster candidates in the optically selected catalogues will now be presented. Since the vast majority of the optically selected clusters have no X-ray selected counterparts, fluxes/flux limit were measured at the positions of the optical candidates.

Aperture fluxes were measured from the X-ray images. The peak X-ray flux within a 1.5 arcmin search radius was located, to provide the centre of the measurement. A 1.5 arcmin radius aper-

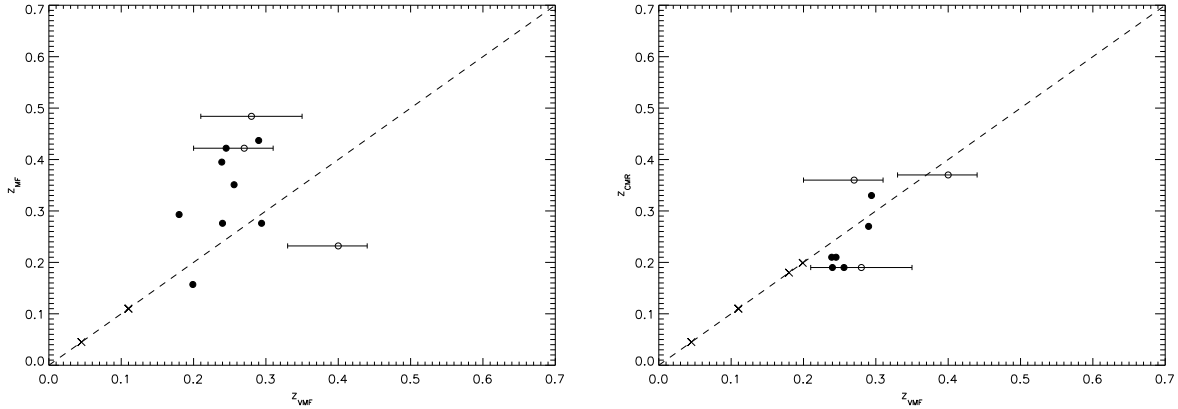


**Figure 14.** Comparison of the optical cluster finders' redshift estimates with Vikhlinin et al.'s redshifts. Open symbols are for VMF photometric redshifts with error bars showing their estimated range; filled points are for spectroscopic redshifts. Dashed line shows the one to one relation, and crosses on this line indicate undetected clusters. These numbers are tabulated in Fig. 3. The CMR redshift appears to systematically underestimate the VMF spectroscopic redshift by  $\approx 0.03$ , in all but one case. This is for VMF86 which is in fact two systems, as indicated earlier. The more significant candidate happens to be the higher redshift one, but if VMF measured a redshift for the lower redshift system, then this too would be underestimated by a similar amount.

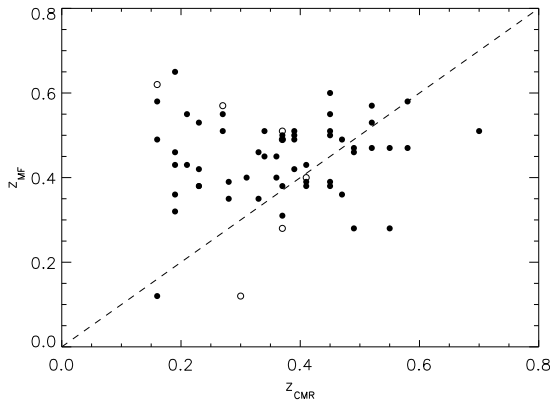


**Figure 15.** Comparison of MF and CMR estimated redshifts. Filled points are unique matches; open points are flagged as line of sight projections in the CMR catalogue. Dashed line is the one to one relation.

ture was used. This aperture flux was then corrected to a total flux computing the ratio of total flux to flux within the 1.5 arcmin radius aperture for a cluster beta model of typical parameters. This method is a compromise between choosing too large an aperture and increasing the chance of background contamination from point sources, and choosing too small an aperture and missing cluster flux. This aperture was found to give the best agreement with the wavelet X-ray flux measured by Vikhlinin et al. (1998) (Fig 16). Also tried was the use of a standard maximum likelihood technique to fit a cluster beta model to the X-ray surface brightness profile, but this gave largely poor fits, as the systems we detect are not well-matched to the standard model assumptions used (such as spherical symmetry).

The ROSAT count rate in the 0.5–2.0 keV band was converted to a bolometric luminosity correcting for the observed Galactic hydrogen column density, assuming the CMR estimated redshift and assuming a cluster temperature of 5 keV. The luminosity was then iterated once by assuming a fit to the X-ray luminosity temperature relation given by  $T_x = 2.75(L_{bol,X}/h_{50}^2)^{0.357}$  (a compendium from Reichart et al. 1999; Arnaud & Evrard 1999;

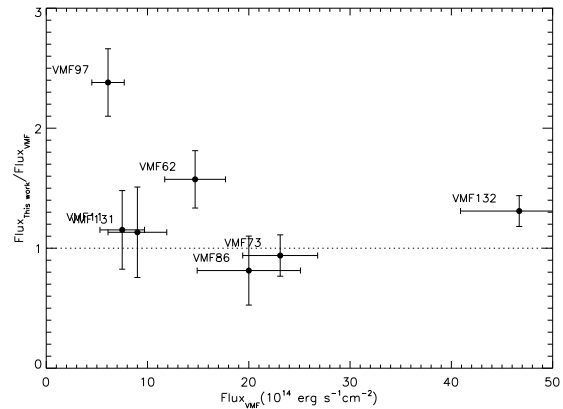


**Figure 16.** Comparison of our aperture X-ray fluxes with the wavelet fluxes of VMF98 for clusters in common with their sample. VMF IDs are indicated.

Markevitch 1998; Allen & Fabian 1998). This has little effect on the resulting luminosity. The background flux rate was determined for each object by the maximum likelihood method in which it was a free fitting parameter. The background flux rate was also measured for each field by placing 100 apertures randomly around each image and measuring fluxes in the same way.  $3\sigma$  outliers were rejected from these estimates to obtain the median and variance. The background values obtained by both methods agreed well with each other. The significance of each optical candidate X-ray flux measurement was determined relative to the variance of the background flux measurements in each field. If the measurement was a greater than  $3\sigma$  event, this was classed as a detection. For other measurements, a  $3\sigma$  upper limit was found from the limiting flux for the field. The typical  $3\sigma$  limiting flux is around  $6 \times 10^{-14}$  erg s $^{-1}$  cm $^{-2}$ . X-ray detections at  $\geq 3\sigma$  were visually inspected, and those showing contamination from an obvious bright point source were rejected from the analysis. 40 of the 290 apertures resulted in  $\geq 3\sigma$  X-ray detections.

A plot of each of the richness measures described in §4 versus the X-ray luminosity is given in Figs. 18 and 19.

Firstly we consider the relation between the total early type galaxy luminosity,  $L_E$  and X-ray luminosity,  $L_X$ . The two quantities appear to be correlated, but with large intrinsic scatter. One concern about plotting two measures of luminosity against each other is the fact that the two are correlated through the distance to each object. In order to show that this is not producing the observed correlation, Fig. 20 shows the ratio of the two luminosities as a function of redshift. This distance-independent measurement shows that there is still an intrinsic scatter in the luminosities at each redshift interval. We use a Bayesian maximum-likelihood technique to fit the relations shown in Figs 18, 19. We assume that there is a power-law correlation between  $L_e$  and  $L_X$  with a large intrinsic scatter ( $\sigma$ ), which we assume to be Gaussian in  $\log L_X$ , and is independent of  $L_e$ . There are three model parameters that must be determined: the normalisation and exponent of the mean relation, and the scatter about the relation. The statistical problem is an unusual one because the upper limits far outnumber the detections. Furthermore, the scatter in the relation is much larger than the errors in the measurements. To simplify the fitting procedure, we therefore treat the measurement errors as a component of the scatter in the model relation.

We tried three methods of fitting the data. Firstly, we can use only the X-ray detections. This gives  $L_X = 10^{-0.338} L_E^{0.94}$ , but this model relation fails to take any account of the large number of upper limits. Secondly, we can incorporate the upper limits by treating the limit as a data point. We eliminate the data points flagged as contaminated by point sources from this fit. This gives a relation that has lower normalisation and larger scatter. Our ML estimator gives similar results to conventional regression schemes in both these cases. However, while the second approach takes into account the upper limits, it does not allow for the possibility that the actual  $L_x$  might lie significantly below the upper limit. Finally, we apply our maximum-likelihood estimator, treating the upper limits correctly. We must make two Bayesian assumptions to apply the method: (1) we assume that the probability distribution for the value underlying an upper limit is uniform in  $L_x$  (rather than  $\log L_x$ ); (2) we allocate greater prior weight to models with small scatter by introducing a prior weighting  $P_{prior}(\sigma) \propto \frac{1}{\sigma}$ . This is appropriate to values bounded between 0 and  $\infty$  and gives equal probability per decade in  $\sigma$ . Without this assumption (and since upper limits greatly outnumber detections), the likelihood estimator gives too much weight to models with very high scatter and very low normalisation. This results in the relation  $L_X = 10^{-0.740} L_E^{0.84}$ , with a scatter of  $10^{0.23}$ . The effects of the different fitting techniques are illustrated in Fig. 17. A similar method for the  $B_{gc}$  parameter results in the relation  $L_X = 10^{-5.08} B_{gc}^{1.59}$ , again with a scatter of  $10^{0.23}$ , fitting both detections and limits with this Bayesian approach.

In addition, the richness measure  $N_{0.5}$  (Bahcall 1981) similar to the Abell Richness Class, was studied and found to give an unusably large scatter. Yee & López-Cruz (1999) also found this measure gave unacceptable scatter.

Examples of outliers in these relations are now considered, to assess if clusters with similar richnesses do indeed exhibit very different X-ray luminosities. The candidates listed in Table 4 are chosen as obvious outliers in the  $L_X$ - $L_E$  plot. For brevity, the candidates are referred to as A, B, C, D. For each of these, an I-band image with X-ray contours overlaid and a CMD with the fitted CMR overlaid is shown (Figs 21-24), to verify the properties which locate them in the  $L_X$ - $L_E$  plot. Candidate A is one of the least X-ray luminous candidates, but is also not very optically rich. Candidate B is highly X-ray luminous and of moderately high

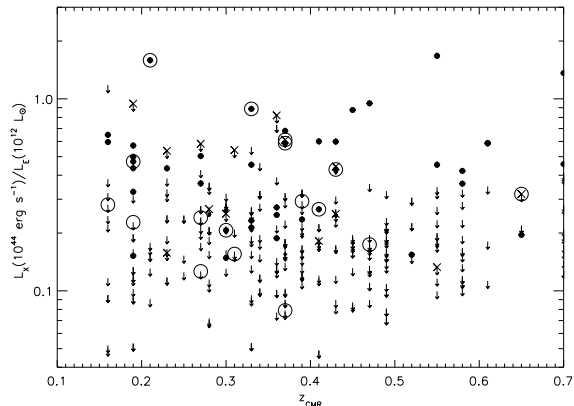


**Figure 20.** X-ray luminosity /  $L_E$  as a function of CMR-estimated redshift. Symbols as for Fig. 18.

**Table 4.** Table of properties for interesting outliers from  $L_X$ - $L_E$  relation. Letter preceding candidate ID is for brevity when discussing these case studies in the text.

Candidate ID	$L_X^{44}$	$L_E^{12}$	$B_{gc}$	$z_{est}$
A – cmJ072345.2+712742	$\leq 0.06$	0.7	500	0.16
B – cmJ162617.5+781706	6.5	3.9	720	0.55
C – cmJ131148.5+322803	25.3	18.6	—	0.70
D – cmJ032903.1+025640	$\leq 0.4$	4.0	1100	0.37

optical luminosity, laying just above the  $3\sigma$  upper bound of the relation. Candidate C is the most X-ray luminous and optically luminous candidate; and candidate D has a comparable richness to candidate B, but is an order of magnitude less X-ray luminous.

The two high  $L_X$  systems (B and C) indicated have very different optical richnesses. Due to the volume probed and the rarity of such luminous clusters, these systems are expected to be at the high redshift end of the survey (the volume between  $0.2 < z < 0.5$  is similar to that between  $0.5 < z < 0.7$ ) and, indeed, they are both found to lie in the range  $0.5 < z < 0.7$ . Conversely, in order to be detected, the faintest systems must lie at low redshift (A). The fairly optically rich system with a low X-ray upper limit (D) lies intermediate in redshift to these extremes.

From these figures (21 – 24), the example cluster candidates appear to have the properties measured in the catalogues and shown in Table 4. For example, the X-ray detections do not appear contaminated by point sources, and the redshift estimates seem entirely consistent with the predicted CMRs.

Cases B and D have similar  $L_E$  values, but their X-ray luminosities vary by over an order of magnitude. Examining the relation using  $B_{gc}$  instead of  $L_E$  shows that both these systems occupy similar regions of this plot.

The scatter in the relation could be attributable to a number of factors. The physical processes involved in the determination of  $L_X$  have been discussed in §1, but will be reiterated here, along with a discussion of  $L_E$ . The X-ray luminosity is dependent on the temperature and density of the gas. These in turn depend on the dynamical state of the cluster (which determines the depth of the gravitational potential, and the densities that can be reached by the gas). The presence of a cooling flow increases the luminosity by increasing the gas density.  $L_X$  can also be increased through unresolved point source contamination.

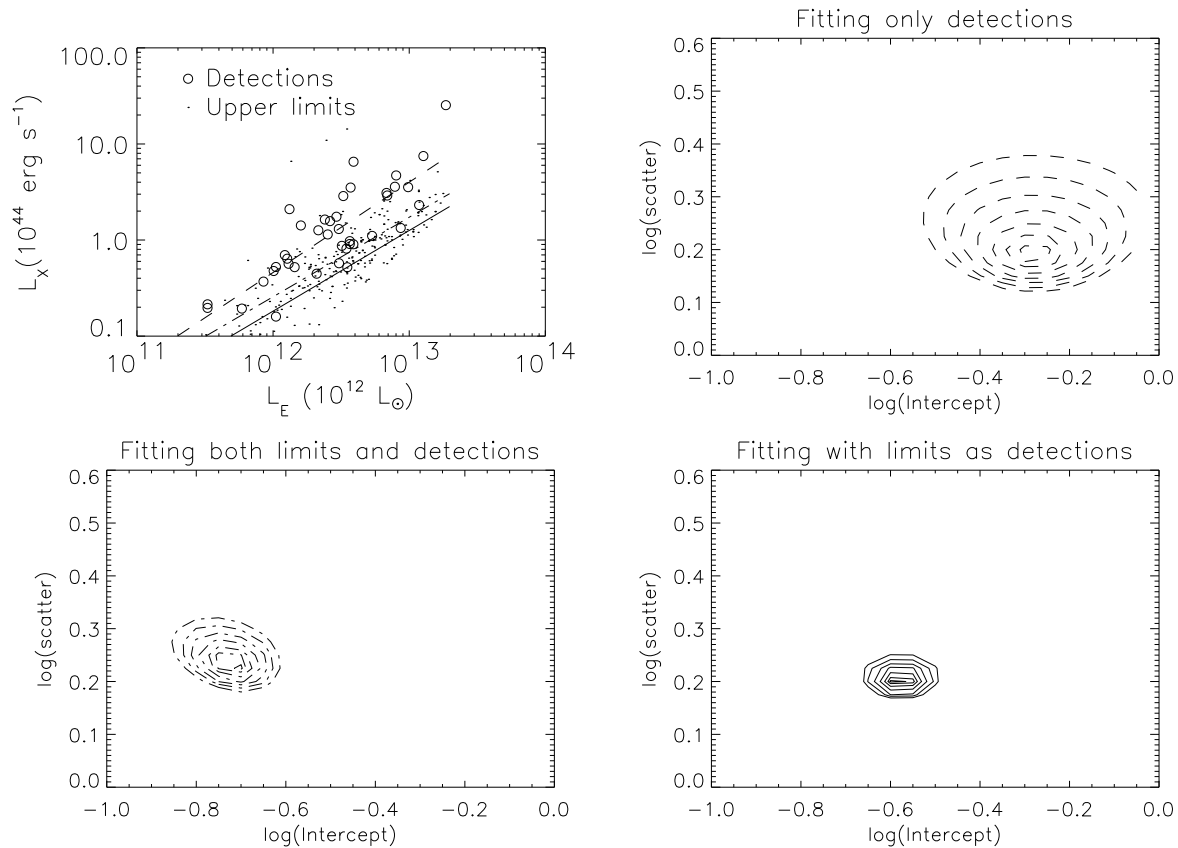


**Figure 17.** Results of different fits to the  $L_X - L_E$  relation. The data are shown in the upper left panel with detections as open circles and upper limits as points, for clarity. Overplotted lines show the different fits in the same line style as the contour plots. Contours show confidence limits for the fitted scatter and intercept (at  $L_E = 10^{12} L_\odot$ ) – upper right panel: fitting only the detections; lower left panel: fit to upper limits and detections, using Bayesian approach described in text; lower right panel: all points fitted assuming upper limits are detections (this is essentially the same as assuming detections would lie just below the limits). Confidence levels run from  $1-\sigma$  to  $7-\sigma$  in  $1-\sigma$  intervals.

The optical properties of the cluster candidates obviously depend on the properties of the member galaxies. Since these systems were selected on the presence of a CMR, a population of galaxies which formed their stars at high ( $z > 2$ ) redshift, and terminated star formation shortly after, is required.

The interplay between the intracluster medium and the cluster galaxies is likely to be important and not straightforward to model. Several workers (e.g. Ponman et al. 1999; Bower et al. 2001) have recently investigated such interplay using numerical simulations. They propose energy injection at early times from supernovae in cluster galaxies as a method to ‘pre-heat’ the ICM and produce observed relations such as the  $L_X - T_X$  relation. It is then quite likely that the scatter comes from variation in the X-ray luminosity rather than the mass to galaxy luminosity conversion.

## 7 SPECTROSCOPIC OBSERVATIONS OF X-RAY DARK CLUSTER CANDIDATES

In order to confirm the reality of candidate cluster systems from the XDCS, follow-up multi-object spectroscopy was undertaken with the MOSCA<sup>3</sup> instrument on the Calar Alto 3.5m telescope.

MOSCA is a focal reducing spectrograph, installed at the Richey-Chretien Focus of the 3.5m telescope on Calar Alto. The reduction ratio of the optical system is 3.7, i.e. the effective focal ratio is  $f/2.7$ . This gives an image scale of 3 pixels per arcsec and a total FOV of  $11 \times 11$  arcmin. A thinned CCD with  $2048 \times 4096$  15 micron pixels is used as the detector. The med-green grism was selected. This gives a wavelength coverage of 4300 - 8200Å, with a central wavelength of 5500Å and a dispersion of around  $2.5\text{Å}/\text{pixel}$  and resolution of around  $10\text{Å}$  FWHM. This allows distinctive spectral features to be seen over a wide range of redshifts from  $z \lesssim 0.1$  to  $z \gtrsim 0.6$ .

Cluster candidates with no extended X-ray counterpart, detected in the Vikhlinin et al. (1998) catalogue fields were chosen. The only other criterion applied was that the RA range available for the observing run meant that the candidates had to come from the subset of XDCS originally observed during the June 1998 run. This subsample comprises 16 fields, or approximately 4.5 square degrees. These targets are listed in Table 5. For each one, astrometry was performed using the STARLINK program ASTROM to convert pixel coordinates into sky coordinates as measured from the APM catalogue<sup>4</sup>, to an *rms* accuracy of of  $\approx 0.3$  arc seconds. Multi-object slit masks were constructed using a constant slit width of 1.5 arcsec and a slit length of at least 10 arcsec. In order to be included

<sup>3</sup> <http://www.mpia-hd.mpg.de/MOSCA/index.html>

<sup>4</sup> <http://www.ast.cam.ac.uk/~mike/apmcat/>

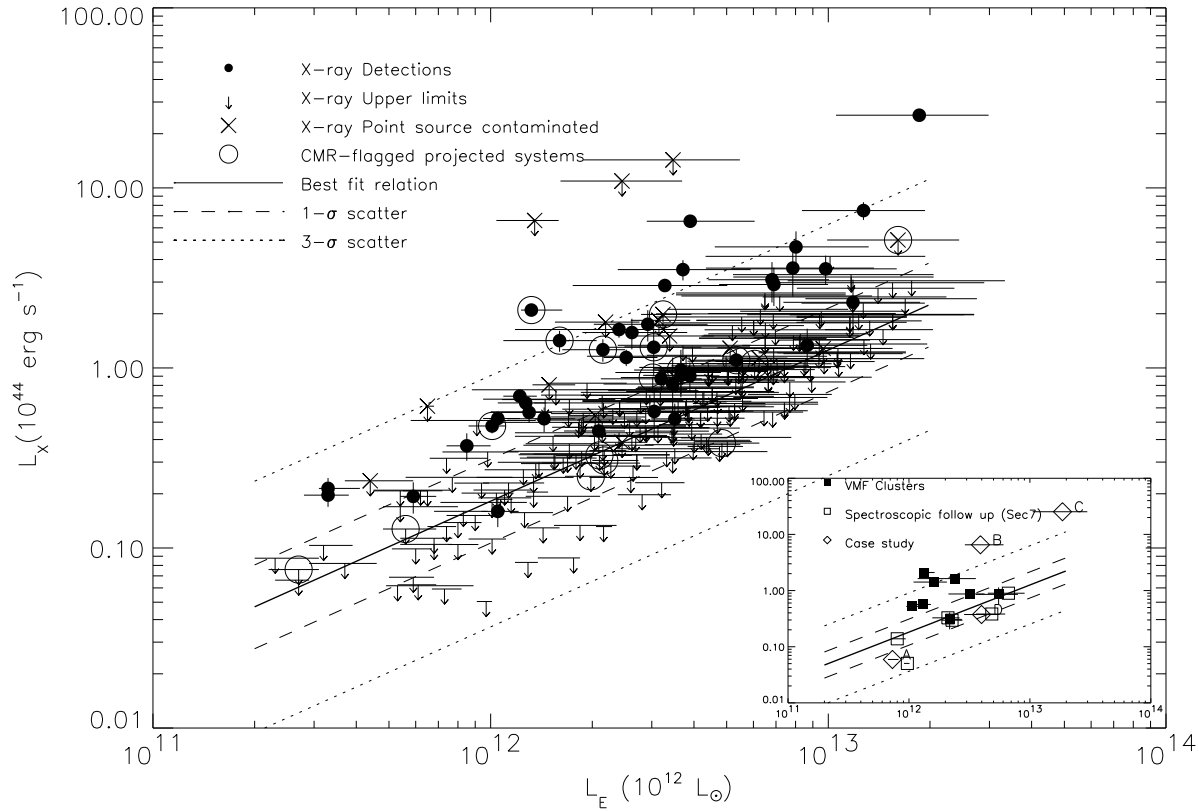


**Figure 18.** X-ray luminosity vs the  $L_E$  richness measure. Filled points are  $>3\sigma$  X-ray detections; downward arrows are  $3\sigma$  upper limits. Solid line is the best fit relation of the detections and limits using the Bayesian technique described in the text. Inset shows specific systems which are further discussed in text.

**Table 5.** MOSCA mask centres. Note: the IDs are just numbered subfields of the RIXOS fields, and should not be confused with the similar nomenclature used for X-ray candidates by the RIXOS collaboration.

Candidate	$\alpha$ (J2000)	$\delta$ (J2000)
R110_1	14 28 22.0	+33 07 13
R220_2	17 23 37.9	+74 43 17
R236_1	17 02 58.9	+51 53 52
R294_1	23 19 54.5	+12 32 27

as potential slit candidates, galaxies had to be brighter than  $I_C=20$  (often a few galaxies fainter than this were allocated slits to fill the masks).

### 7.1 Spectroscopic Observations and Data Reduction

The spectra were secured over six nights of observations in July 2000 using MOSCA on the Calar Alto 3.5m. A log of the observations is presented in Table 7.

Before each night of observation, a series of bias frames (typically five) was taken. For the purpose of wavelength calibration (WLC) two different comparison arcs were observed. This was done to ensure an adequate number of emission lines over the full-wavelength range covered by the MOSCA med-green grism. A 15s

**Table 7.** Log of observations of cluster candidates from Calar Alto.

Night	Field	Mask	Exposure time (s)
27 – 28/07/00	R110_1	1	$3 \times 1800$
28 – 29/07/00	R236_1	1	$3 \times 1800$
29 – 30/07/00	R220_2	2	$2 \times 1800$
29 – 30/07/00	R236_1	2	$3 \times 1800$
30 – 31/07/00	R294_1	1	$3 \times 1800$
31/07 – 01/08/00	R294_1	2	$3 \times 1800$

exposure of the HgAr/Ne arc was taken. This was augmented by a 120s exposure of the Ar lamp using the 472/78 filter. The long exposure was used to make weak emission lines clearly visible, and the (BV-band) filter was used to suppress lines at the red end of the spectrum, which would otherwise become saturated. A combination of the HgAr/Ne spectrum and  $100\times$  the Ar spectrum was found to provide a good reference spectrum for WLC (hereafter, WLC refers to this composite arc spectrum image). Such calibration frames were taken before twilight, at the start of each run. Flat-field frames were taken using MOSCA’s internal tungsten lamp. For the science observations, three exposures were made of each mask, each of 30 minutes duration. After each series of science frames, whilst the telescope was still pointing at the object, another HgAr/Ne frame was taken (although it was not needed, see later). This was done in case flexure in the instrument due to the telescope’s different pointing position affected the arcs taken earlier in the evening (while the telescope was parked, and therefore point-

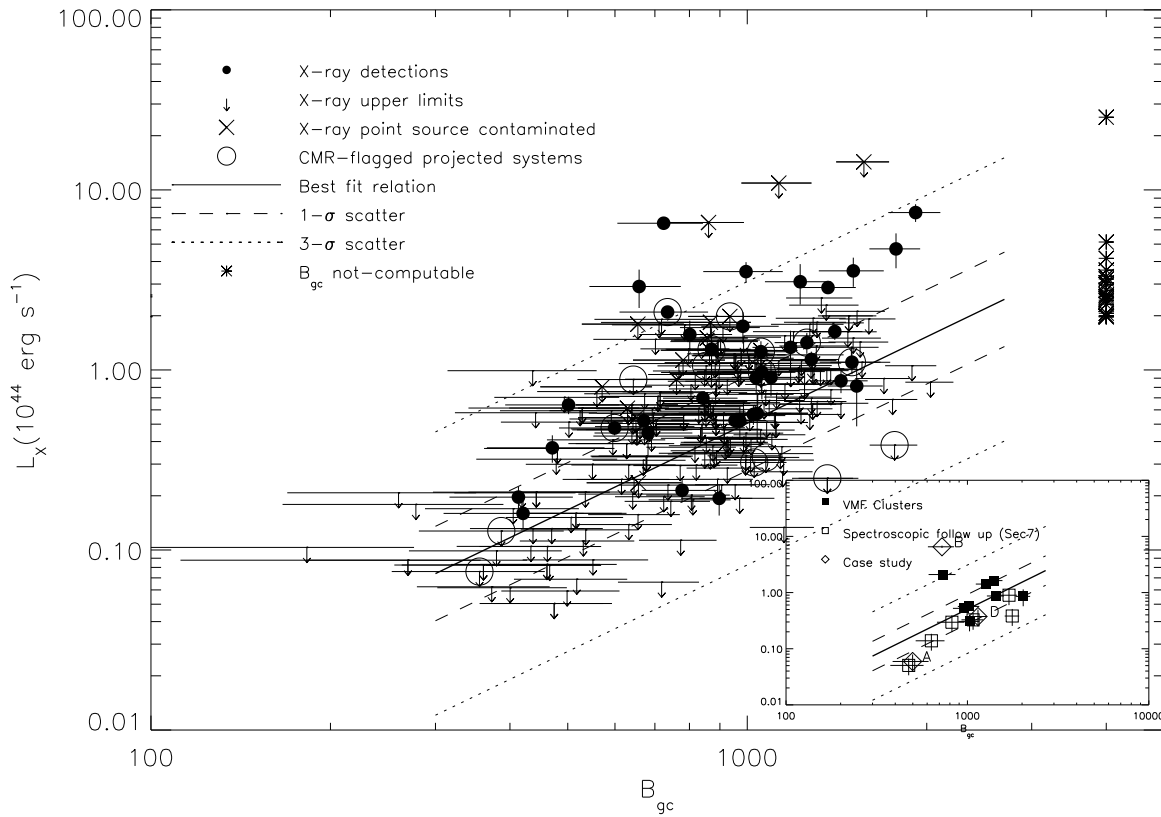


**Figure 19.** X-ray luminosity vs the  $B_{gc}$  richness measure. Filled points are  $>3\sigma$  X-ray detections; downward arrows are  $3\sigma$  upper limits. Solid line is the best fit relation of the detections and limits using the Bayesian technique described in the text. Inset shows specific systems which are further discussed in text (note: a  $B_{gc}$  value could not be computed for case study C).

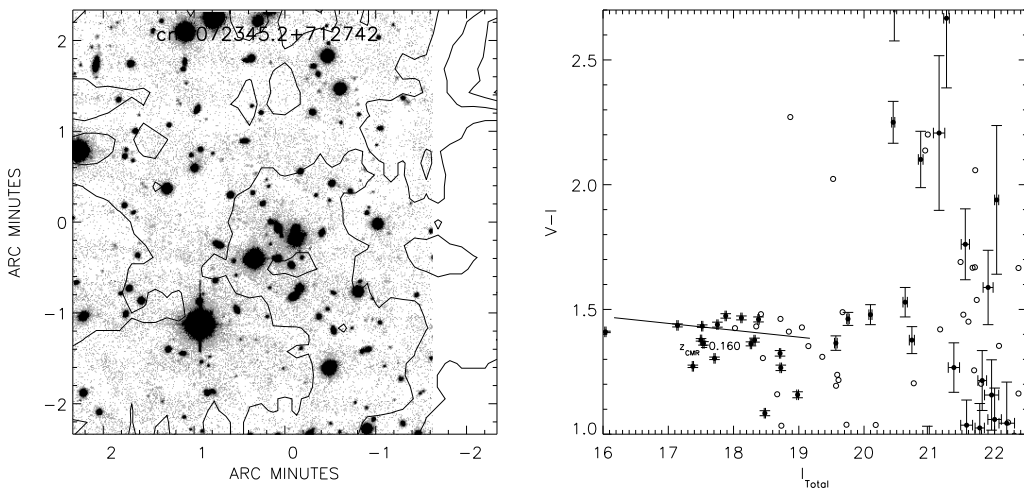


**Figure 21.** Plots as for Fig. 12 for case study A (candidate cmJ072345.2+712742). Solid line in CMD indicates model CMR for estimated redshift.  $z_{CMR} = 0.16$ . This system is X-ray underluminous, and of reasonably low optical luminosity.

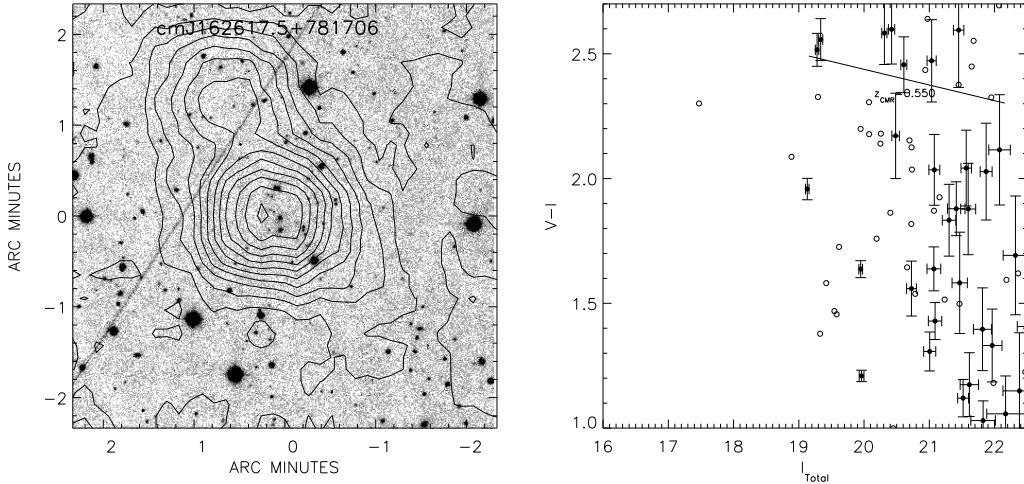


**Figure 22.** Plots as for Fig. 12 for case study B (candidate cmJ162617.5+781706).  $z_{CMR} = 0.55$ . This is a fairly optically luminous system with a very high X-ray luminosity for its richness.

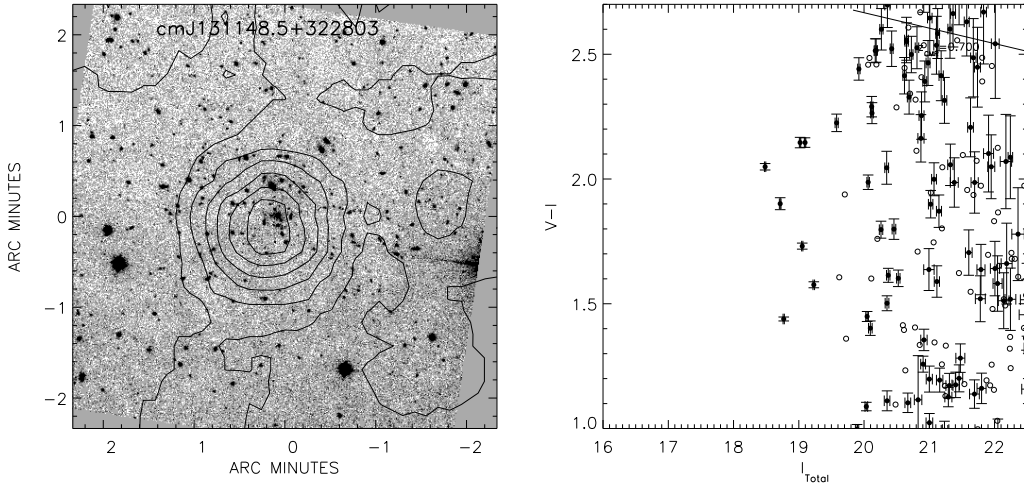


**Figure 23.** Plots as for Fig. 12 for case study C (candidate cmJ162617.5+781706).  $z_{CMR} = 0.70$ . This is a high redshift, optically rich candidate with very high X-ray luminosity.

ing at zenith). The Ar arc was not repeated during the night as its longer exposure time added an unacceptable overhead.

### 7.2 Data Reduction

Data reduction was carried out using standard IRAF routines. Master biases were created for each night by combining several bias images. Full 2D bias removal was necessary as the bias frames displayed banded structure. Flatfielding was attempted but found to offer no improvement in the identification of spectral features and so was omitted. The three science exposures of each image were averaged to reject cosmic rays. The spectra were then extracted using

apall. Wavelength calibration was carried out using the composite arcs. No flux calibration was performed.

### 7.3 Spectroscopic Redshift Determination

The Fourier cross-correlation technique of Tonry & Davis (1979) was applied to the wavelength-calibrated spectra. This technique continuum-subtracts and Fourier transforms the galaxy spectrum and a reference template, applies high- and low-pass filtering, and looks for peaks in the cross-correlation function of the two.

The template used was a de-redshifted E/S0 (as used by the CNOC collaboration, courtesy of E. Ellingson), hence no emission

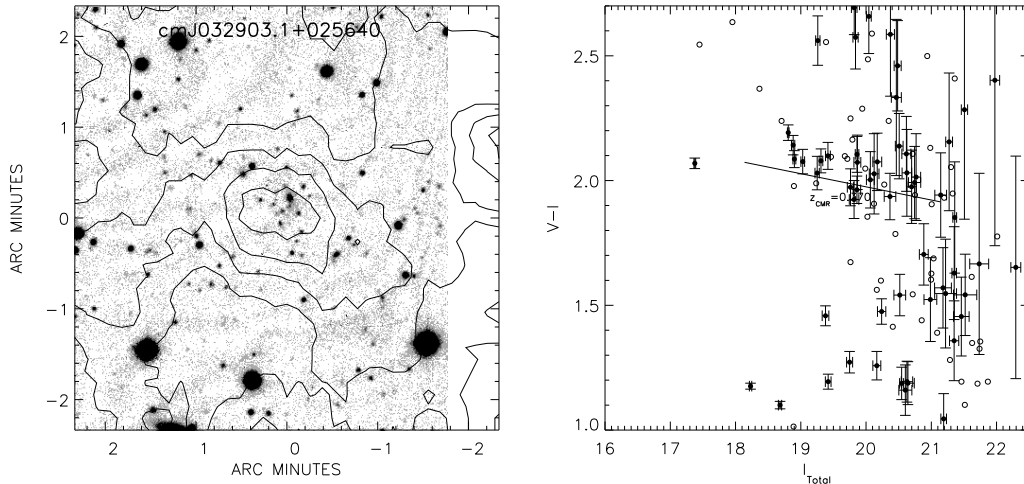


**Figure 24.** Plots as for Fig. 12 for case study D (candidate cmJ032903.1+025640).  $z_{CMR} = 0.37$ . This is a candidate of similar optical richness to case B (at slightly lower redshift; 0.37 vs 0.55) but with an order of magnitude lower X-ray luminosity.

**Table 6.** XDCS CMR candidates in MOSCA Fields. Dist indicates distance from field centre.  $\ddagger$  - (p) in estimated redshift indicates that candidate is flagged as a line-of-sight projection by the method described in §4.1. X-ray fluxes and luminosities (using estimated redshifts) are  $3\sigma$  upper limits for all candidates, none of which is detected in X-rays.

Field	XDCS ID	Dist (arcmin)	$z_{est} \ddagger$	$F_X$ ( $10^{-14} \text{ erg s}^{-1} \text{ cm}^{-2}$ )	$L_X$ ( $10^{44} \text{ erg s}^{-1}$ )
R1101	cmJ142812.0+330736	2.1	0.160	$\leq 3.0$	$\leq 0.02$
R2202	cmJ172333.0+744410	1.0	0.210	$\leq 4.5$	$\leq 0.06$
R2361	cmJ170244.2+515539	2.9	0.310 (p)	$\leq 4.6$	$\leq 0.32$
R2361	cmJ170232.6+514922	6.1	0.300	$\leq 5.1$	$\leq 0.29$
R2361	cmJ170258.9+514921	4.5	0.470	$\leq 3.4$	$\leq 0.90$
R2941	cmJ231951.2+123208	0.9	0.370 (p)	$\leq 2.0$	$\leq 0.08$

lines were used in the initial redshift determination (emission line objects are considered below). Each mask was run through `fxcor`, and the redshift from the highest cross-correlation peak logged. Each spectrum was then de-redshifted using the `fxcor` redshift. The de-redshifted spectrum then had the position of prominent absorption lines (Ca H+K, G-band, H-beta and Mg $\beta$ ) and emission lines OII and H $\beta$  overplotted. The spectrum was then visually inspected and a quality flag assigned to it, either: 2 - the redshift is confident; 1 - the redshift is less certain but looks compatible with the positions of the lines; or 0 - no redshift is possible (usually due to too low S/N).

Some spectra were also flagged for re-processing through `fxcor`, if the redshift was clearly wrong, and sufficient signal was present to get a better redshift estimate. The main reason for an incorrect redshift was the presence of large residuals from the subtraction of bright night sky lines. Note that in the Fourier cross-correlation, the direction (i.e. absorption or emission) of lines is not taken into account; therefore, night sky residuals which approximate the positions of absorption features in the template can be confused.

Absorption lines in the galaxy spectrum were logged, and if a possible emission line was present, the 2D spectrum was inspected

to check if the emission was a genuine galaxy feature, or a residual sky line.

For several spectra, for which the redshifts were readily apparent, and very strong emission was seen, the E/S0 template gave a poor redshift estimate. In this case an Sab/Scd template was substituted and was found to give a much better fit. Emission line objects are clearly noted in the tables of results, below.

Furthermore, once groupings in redshift space had been located (§7.4), all the spectra which failed to yield a redshift were re-examined to see if they were compatible with the redshift of any groupings. This yielded one extra redshift which had been missed previously.

All redshifts were confirmed by visual inspection, by overplotting the spectral features shown in Fig. 25 on the de-redshifted spectra. In order to be considered a confident redshift, two or more spectral lines had to be clearly visible and other features had to have some good reason for not being seen (e.g. strong sky residuals concealing a feature which should have been present).



**Table 9.** Galaxy Groupings in Redshift Space

Field	Galaxy grouping	Centroid <sup>a</sup>		N <sup>b</sup>	N <sub>TOT</sub> <sup>c</sup>	median z	$\Delta z^d$	N <sub>Absp</sub> <sup>e</sup>
		$\alpha$ (J2000)	$\delta$ (J2000)					
R110_1	1a	14 28 27.9	33 05 24	3	8(13)	0.196	<0.001	3
R220_2	2a	17 23 25.1	74 43 45	7	14(21)	0.260	0.003	5
R236_1	3a	17 02 59.2	51 53 25	6(7)	24(30)	0.297(0.297)	0.007(0.007)	3(4)
R236_1	3b	17 02 52.4	51 54 00	11	24(30)	0.347	0.004	11
R294_1	4a	23 20 00.2	12 32 06	3	17(25)	0.268	0.001	1
R294_1	4b	23 19 48.0	12 32 58	3	17(25)	0.325	0.003	3
R294_1	4c	23 19 55.6	12 32 20	5	17(25)	0.454	0.010	4

<sup>a</sup> Centroid of members of grouping, using class 2 redshifts.

<sup>b</sup> Number of galaxies in grouping – class 2 spectra (class 1 & 2 spectra).

<sup>c</sup> Total number of class 2 (class 1 & 2) spectra in field.

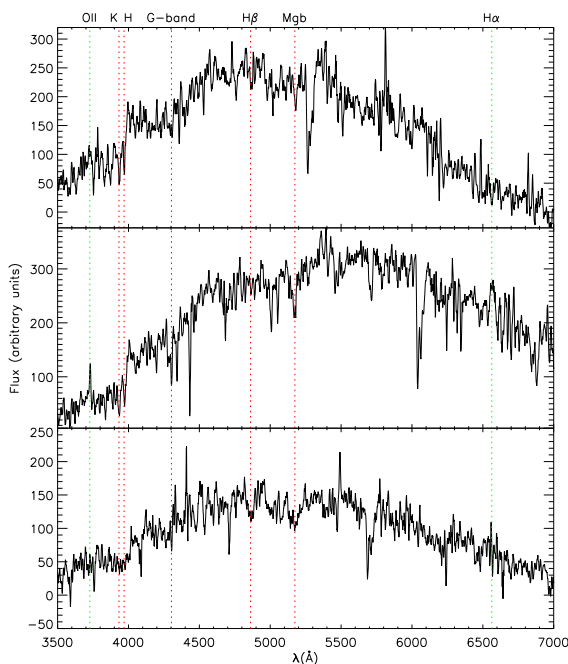
<sup>d</sup> Maximum redshift separation between a galaxy in the grouping and the median redshift of the grouping.

<sup>e</sup> The number of absorption line only (i.e. no emission) galaxies in the grouping.

Note: galaxies must be within 1500 km s<sup>-1</sup> in the rest-frame, at the median redshift, to be considered members of the grouping (see text).

**Table 8.** Summary of Spectral Quality. 2 - secure redshift; 1 - less confident; 0 - rejected.

Field	Number of Spectra		
	Class 0	Class 1	Class 2
R110_1	2	5	8
R220_2	14	7	14
R236_1	8	6	24
R294_1	7	8	17


**Figure 25.** Representative de-redshifted spectra. From top to bottom: spectrum with confident redshift; spectrum with confident redshift and emission lines; spectrum with less confident redshift.

#### 7.4 Significance of Clustering in Redshift Space

Groupings in redshift space were extracted by searching for 3 or more secure redshifts separated by 1500 km s<sup>-1</sup> or less. This is the same method adopted by Holden et al. (1999) and corresponds to 3 × the typical cluster velocity dispersions they measured. It should be noted that a larger value was also tried, but 3 $\sigma$  clipping (described later) removed any extra galaxies added. The results of groupings found by this technique are illustrated in Fig. 27 and analysed below.

Ramella et al. (2000) and Holden et al. (1999) used similar techniques to assess the significance of clustering in redshift space. Ramella et al. (2000)'s method is followed here. The selection function was calculated as follows. Fig. 26 shows the number of galaxies for which redshift measurements were possible, as a function of magnitude. Henceforth, only secure redshifts will be considered. Note that all cluster members in the sample are class 2 (i.e. secure) redshifts, except one which is class 1. Of the 121 spectroscopic targets, 61 resulted in secure redshifts, and a further 26 with less secure measurements. Two of these objects were stars. The majority of galaxies which fail to yield a redshift are fainter than  $I_c = 20.0$ .

As with the 2D data in §3.1.4, it is important to model the clustering of field galaxies when constructing mock galaxy distributions. By using the Canada France Redshift Survey (CFRS, Lilly et al. 1995) to construct a simulated field redshift distribution (as was done by Holden et al. 1999), and bootstrap resampling sets of galaxies, an estimate can be made of the fraction of spurious clustering detected in redshift space. Sets of 15 galaxies were extracted - the mean number per field (2 masks) for which confident redshifts were secured. 10000 galaxy sets were generated, applying bootstrap resampling, and the fraction of sets containing a grouping of more than 4 galaxies within 1500 km s<sup>-1</sup> of their median redshift found. This occurs by chance ~6% of the time. For field R110\_1, only 3 galaxies were found within this velocity difference, but fewer than average redshifts (8) were obtained (due to only one, rather than two, masks being used). The velocity difference between these 3 is less than 1000 km s<sup>-1</sup>. This also occurs about 6% of the time, and is therefore approximately as significant. If the

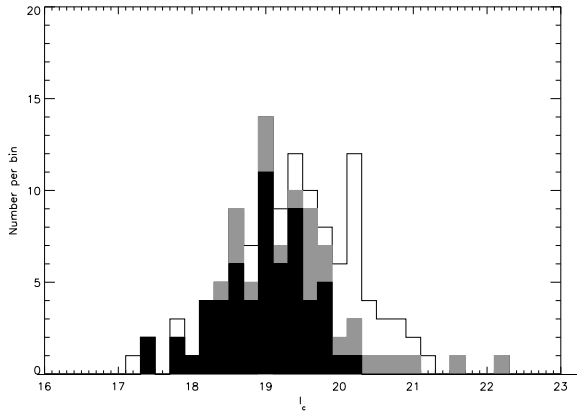


**Figure 26.** The I-band magnitude distribution of galaxies for which spectroscopy was attempted. The empty histogram shows galaxies for which no redshift was determined; the black histogram shows galaxies with confident redshifts; and the grey histogram shows galaxies with less confident redshifts.

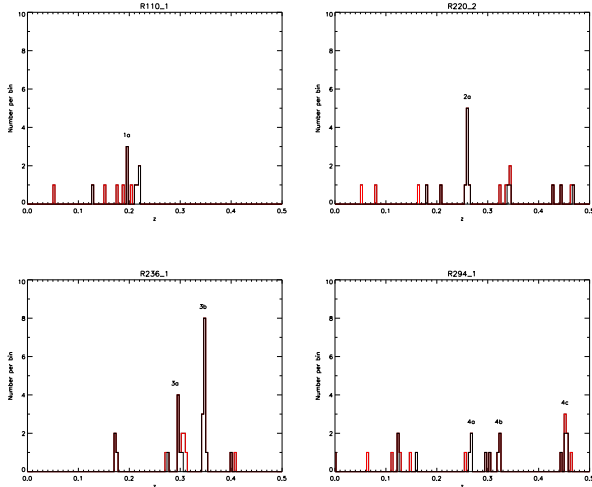


**Figure 27.** Large scale redshift distributions for cluster candidates: R110\_1 (upper left), R220\_2 (upper right), R236\_1 (lower left), R294\_1 (lower right). Line thickness indicates confidence in the redshifts. Bold lines are confident redshifts. The bin size is 0.004, which corresponds to a rest frame velocity of 1200 to 800  $\text{km s}^{-1}$  at the left and right sides of the plot, respectively.

velocity difference is reduced to 1000  $\text{km s}^{-1}$ , the likelihood of finding 4 or more galaxies this close together in an observation of a 15 galaxy set is only 2%. These numbers are used as a guideline to the significance of groupings in redshift space.

Ramella et al. (2000) take this technique further by trying to reproduce more accurately the magnitude selection function. To do this they take the histogram of magnitudes for which spectra were obtained and divide this by the total number of galaxies in the same area in the same magnitude bin (i.e. the histogram shown in Fig. 26 is divided by the field galaxy number counts - Fig. 2 - the result is shown in Fig. 28).

If the luminosity function is universal and the local normalisation is the same everywhere (i.e. no clustering), then the redshift distribution is given by:

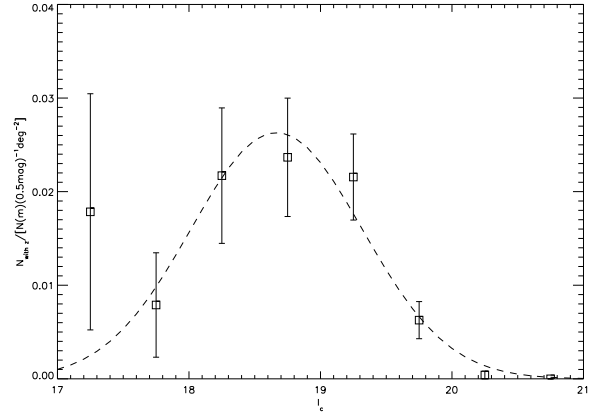


**Figure 28.** The magnitude selection function,  $s(m)$ , for our spectroscopic sample. See text for details.

$$N(z) = \frac{dV(z)}{dz} \int_{m_1}^{m_2} f[L(m, z)] s(m) dm \quad (10)$$

(Ramella et al. 2000) where  $dV$  is the volume element,  $m_1, m_2$  are the magnitude limits and  $f$  is the Schechter LF given in §3.1.2. Applying the selection function,  $s(m)$  gives the redshift distribution shown in Fig. 29. Ramella et al. (2000) note that using such a distribution gives a false impression of the significance of groupings, as the clustering in redshift space must be accounted for. In order to do this, the CFRS is again bootstrap resampled, but this time using the magnitude selection function  $s(m)$ . In Ramella et al. (2000)'s method, they compare the  $N(z)$  distribution of their data with that of the CFRS using their selection function, and state that a Kolmogorov-Smirnov test shows the two datasets have similar distributions. Using the XDCS spectroscopic sample, however, a KS test shows the bootstrapped CFRS  $N(z)$  and the  $N(z)$  in Fig. 29 are significantly different at the >90% level. It appears that this is because a larger fraction of the redshifts in the XDCS sample are cluster members. The Ramella et al. (2000) sample targeted higher redshift candidates, and so recovered a lower fraction of cluster members than the data presented here (most of the XDCS cluster candidates lie in the range  $0.2 < z < 0.4$ ). Therefore Ramella et al. (2000)'s data follow the CFRS  $N(z)$  as most of their data are field galaxies (so it is correct when they state that magnitude selection is the main process leading to the inclusion of galaxies in the sample). In the XDCS sample, however, significant groupings of 6 or more redshifts (more than the individual groupings in the Ramella et al. (2000) data) are present, and thus the total (cluster + field) sample is not represented by the field survey of the CFRS. This difference in  $N(z)$ 's provides reassurance that significant clusters have been found.

Using Gaussian  $s(m)$  leads to different probabilities of false detections. For  $n_{req}=4$ ,  $P(\text{false})=0.19$ ; and for  $n_{req}=5$ ,  $P(\text{false})=0.03$ . This illustrates that magnitude selection has a big effect on the significance assigned.

To summarise these tests: the CFRS has been used to simulate the redshift distribution of field galaxies. Two different magnitude selection functions have been used to sample this survey. Bootstrap resampling of the data is used to calculate the probability,  $P(\text{false})$ , of incorrectly identifying a grouping of  $n_{req}$  galaxies in redshift space - the galaxies being selected in the same way as for the MOSCA targets. For the simplest selection function (a step function in magnitude, selecting galaxies brighter than  $m_{lim}$ ),

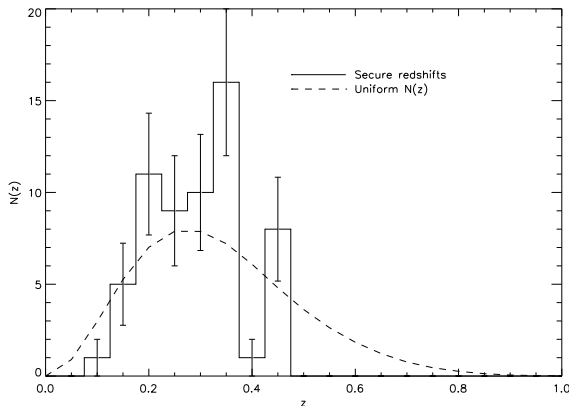


**Figure 29.** The redshift distribution function for our spectroscopic sample. The dashed line shows the  $N(z)$  described by Equation 10.

$P(\text{false}) \approx 0.06$  for  $n_{req} = 4$ . For the best-fit Gaussian magnitude selection function,  $P(\text{false}) \approx 0.19$  for  $n_{req} = 4$ , and  $P(\text{false}) \approx 0.02$  for  $n_{req} = 5$ .

These are the most recent techniques used in the literature for estimating the significance of redshift groupings found from optical cluster surveys. However, there are several problems with them. Firstly, using the CFRS to model the field does not take any account of the presence of groups within it. Thus, for finding the lowest velocity dispersion systems, which will be numerous in any wide-field survey (and therefore the CFRS), these methods underestimate the significance of systems found. Secondly, not all the available information is used. The most basic spectral properties (i.e. whether or not the cluster members possess emission lines) and the colours can be used to infer the types of galaxies in the sample. Absorption line systems with red colours at the given redshift are highly indicative that a galaxy is of early-type. Since these systems dominate the cores of known clusters, but are much less common in the field, their presence increases the likelihood of a cluster. This technique, however, would be biased against systems not containing early-type galaxies.

It should be noted that using a mean  $N(z)$  from many fields would tend to overestimate the significance of clustering found in any one pencil beam survey, especially if galaxies lie in sheets along the line of sight.

By taking the field galaxy luminosity function from the CNOC2 survey (Lin et al. 1999), the expected number of early-type galaxies in a given volume can be calculated. Lin et al. (1999)'s parameters for the  $R_C$ -band luminosity function in the  $q_0=0.1$  cosmology are taken. This is a Schechter LF with two additional parameters to model the evolution in luminosity and density. Lin et al. (1999) state that to convert their LFs to another band, a good approximation is to just apply an appropriate offset in  $M^*$  based on the mean rest-frame colour for that galaxy type. Thus, to calculate the LF at  $z=0.3$  for early-type galaxies, a rest-frame colour of  $R_C - I_C = 0.71$  is used (Kodama & Arimoto 1997) to correct  $M^*$  to the  $I_C$ -band, along with a correction for the different value of  $h$  ( $+5 \log h$ ). The value of  $\Phi^*$  is taken from the  $R_c$  value, only correcting for the  $h$  difference, and applying the evolutionary parameters  $P$  and  $Q$  (Table 2, Lin et al. 1999) to correct to a redshift of 0.3. The difference in  $\Phi^*$  over the range of interest for the extreme XDCS spectroscopic candidates (i.e.  $0.2 \lesssim z \lesssim 0.5$ ) is less than a factor of 2, and so, for simplicity, a fiducial redshift of 0.3 is

used here. This results in a space density of early-type galaxies in the field at redshift 0.3 of  $0.04 \text{ Mpc}^{-3}$ .

The number of galaxies in each redshift grouping showing only absorption features is given in Table 9. Since these systems do not show emission lines and have colours consistent with early-type galaxies at the cluster redshift (Table 9), these are taken to be early-type galaxies. A generous estimate of the volume from which each of these redshift groupings is drawn is to take an angular size of 5 arcmins (approximately the maximum separation on the sky between galaxies in the same redshift grouping) at a redshift 0.3, and to assume the volume is a sphere of this radius (this is about the same size as given by a line-of-sight velocity difference of a  $1000 \text{ km s}^{-1}$ , again a generous value for these groupings). This translates into a volume of  $\approx 8 \text{ h}^{-1} \text{ Mpc}^3$ . Since the space density of early-type galaxies in the field at this redshift is of  $0.04 \text{ h}^{-1} \text{ Mpc}^3$ , the expected number in such a volume is 0.32. Assuming the field can be modelled by a Poisson distribution with this expectation value, the likelihood of finding 11 early-type galaxies (the maximum found - candidate 3b) is only  $\approx 1 \times 10^{-8}$ . The likelihood of finding 1 (the minimum - candidate 4a) is 25%; and the likelihood of finding 3 (the minimum of all the remaining candidates) is 0.3%.

This argument is an over-simplification as firstly it assumes the field can be modelled as a Poisson distribution, which is not strictly correct because of clustering, but not a bad approximation (it just raises the expectation value slightly). Secondly, the candidates were selected to be overdense in galaxies of the same colour. This means the fields selected were not typical regions of space. However, selecting galaxies on the CMR was not guaranteed to select early-type galaxies at the same redshift, but this is the result which was found from the spectroscopy. Therefore, the method is still valid. Thus, by this simple argument, it seems reasonable to assume that all the groups containing at least 3 early-type galaxies are significant. This method therefore rejects grouping 4a. In summary, all the redshift space groupings are found to be significant by this technique, except candidate 4a which contains 3 galaxies, but only 1 of which is early-type (i.e. red and emission-free). This candidate is found to be significant by the previous two methods which do not take colour/ type into account. Clusters of this nature (i.e. not dominated by early-type galaxies) have not been observed before, so this system must be treated cautiously.

## 7.5 Comparison of Significant Redshift Groupings with Cluster Candidates

Now that the groupings in redshift space have been identified and their significances assessed, the final step is to compare these with the candidates detected with the cluster-finding algorithm. Firstly, a simple comparison will be made by just finding the nearest candidate in the catalogue (Table 6) with the centroids of the groupings found with MOSCA (Table 9). These are tabulated below for the CMR algorithm (Table 10).

For the CMR-finder, the offset between measured and estimated redshift for the two isolated groups (R110.1 and R220.2) is  $\Delta z \leq 0.05$  for both. For the multiple systems, although only one estimated redshift is given in the table for each field (for the most significant candidate), these candidates were flagged as line-of-sight-projections in Table 6. The estimated redshift of the most significant CMR candidate is always intermediate between the spectroscopic redshifts, and always  $\leq 0.1$ . The full catalogues may be examined for these projected systems, to see how well these agree with the spectroscopically determined groups.

The full CMR catalogues in the region of the R236.1 and

**Table 10.** Nearest CMR candidate to each MOSCA group.

<sup>a</sup> Separation between the centroid of the spectroscopic grouping and the nearest MF candidate in arc minutes and physical distance (Mpc) at  $z_{spec}$ .  
<sup>b</sup> Spectroscopic redshift of the former grouping.  
<sup>c</sup> CMR estimated redshift  
<sup>d</sup> Difference between these two redshifts.

Field	ID	CMR Candidate ID	Separation <sup>a</sup> (arcmin/ Mpc)	$z_{spec}^b$	$z_{est}^c$	$\Delta z^d$
R110	1a	cmJ142812.0+330736	3.995/0.81	0.196	0.160	0.036
R220	2a	cmJ172333.0+744410	0.670/0.17	0.260	0.210	0.050
R236	3a	cmJ170244.2+515539	3.228/0.88	0.297	0.310	0.013
R236	3b	cmJ170244.2+515539	2.092/0.63	0.347	0.310	0.037
R294	4a	cmJ170248.5+515051	2.187/0.56	0.268	0.370	0.102
R294	4b	cmJ231951.2+123208	1.147/0.33	0.325	0.370	0.045
R294	4c	cmJ231951.2+123208	1.082/0.38	0.454	0.370	0.084

**Table 11.** Groups from the full CMR-catalogue for those systems flagged as “projections”.  $\sigma$  is the significance from the CMR algorithm.

Field	CMR candidate ID	$z_{est}$	$\sigma$
R236A	cmJ170240.9+515512	0.270	5.15
R236A	cmJ170242.7+515222	0.470	4.35
R236A	cmJ170244.2+515539	0.310	5.55
R236B	cmJ170248.5+515051	0.390	4.55
R236B	cmJ170250.6+515506	0.300	6.85
R236B	cmJ170252.1+515717	0.490	4.85
R294B	cmJ231945.8+123304	0.270	4.85
R294B	cmJ231951.2+123208	0.370	5.05

R294\_1 fields are given in Table 11. The candidates are split between A and B rotation results for R236\_1, as here the two rotations overlap<sup>5</sup>. This is not the case for R294\_1.

A cross-correlation analysis between the position of each CMR candidate and each MOSCA candidate (position given by centroid of redshifts), and their respective redshifts, was performed. In this way, the closest match in projected and redshift space was located. Fig. 30 shows this data projected into 2D along a line of constant declination (so the R.A. offset gives the approximate sky-plane offset). It can be seen that, for R236\_1, both the A and B catalogues identify 3 candidates at approximately the same redshifts: two close to the MOSCA groups and one at slightly higher redshift. This illustrates that agreement between the A and B redshift estimates is good, and the agreement with the spectroscopic redshifts is also good ( $\leq 0.05$ ). The possibility of a higher redshift candidate, not reached by the depth of the MOSCA spectroscopy, is likely, given that it is identified independently in both rotations, and because the lower redshift groups agree so well with the spectroscopy. For R294\_1, two candidates are found. Given that the lowest redshift of the three MOSCA groups in this field (4a) is not significant from the space density of early-type galaxies analysis (and will not be found by the CMR algorithm, because it does not contain significant numbers of early-type galaxies), the most likely interpretation is that the CMR-finder detects the two highest redshift groups and underestimates the redshifts of both (albeit by only  $\leq 0.08$ ). Thus, the candidates from the full catalogue are naturally associated with the nearest groups in 2D space, and these are then found to be also the nearest in redshift space. Therefore, the CMR finder performs excellently, correctly finding and separating all the systems identified spectroscopically.

<sup>5</sup> R110\_1 also has overlapping A and B rotation, although the V-band A-rotation data is slightly trailed and so rejected from this analysis.

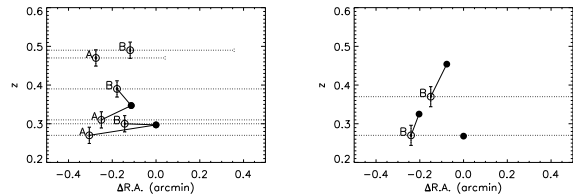


**Figure 30.** R.A. vs  $z$  (declination slice) plot for MOSCA (spectroscopically determined) groups and CMR candidates R236\_1 (left) and R294\_1 (right). Filled circles are MOSCA groups (note: the lowest- $z$  point in the R294\_1 is not significant in terms of early-type galaxies); open circles are CMR candidates from A- and B-rotation data (as labelled). Broken horizontal error bars denote optical radii of candidates (typically  $\sim 1$  arcmin); solid lines connect optical candidates to nearest spectroscopically confirmed group; solid vertical error bars denote width of redshift slice (i.e. CMR estimated redshift error, c.f. Fig. 7). For R236\_1, two candidates in each rotation are seen near the spectroscopically determined group. Also, a higher redshift candidate is seen in both rotations. The spectroscopy may not probe deep enough to have found members of this group. In R294\_1 two candidates are found within  $\Delta z \lesssim 0.08$  of the most significant (i.e. the two highest redshift) spectroscopic groups.

## 7.6 Cluster Velocity Dispersion Estimates

The cluster redshift and velocity dispersion were calculated following Beers et al. (1990). They recommend using the median and standard deviation when dealing with tiny ( $n \sim 5$ ) datasets. Only the secure redshifts were considered. Redshifts within  $\sim 2000$  km s<sup>-1</sup> of the peak in the redshift histogram were extracted and the median value was taken to be the cluster redshift. The standard deviation was computed, and any value exceeding 3 standard deviations from the median excluded (this was only the case for the clusters in field R236\_1: one value was rejected from each), and the standard deviation then re-computed. This was then transformed to the velocity dispersion in the cluster’s rest-frame. The confidence interval for the velocity dispersion was found by applying the statistical jack-knife technique to the data (for example Carlberg et al. 1996). This simple resampling technique uses ‘pseudo-values’  $\delta_i$  of the data, by calculating the difference between a statistical measure,  $f$ , calculated for the whole dataset, and for the dataset with one value removed  $\delta_i = f(x_1, \dots, x_n) - f(x_1, \dots, x_i, x_{i+1}, \dots, x_n)$ . The estimate of the variance is  $[n/(n-1) \sum_i \delta_i^2]^{1/2}$  (Efron 1982). For very small  $N$  ( $\sim 3$ ) this error estimate is likely to be highly biased as only two data points are being resampled each time and the factor of  $\sqrt{n/(n-1)}$  is likely to be an underestimate. These values must be treated cautiously for the three groupings with only 3 galaxies.

As described in §4, Smail et al. (1998) plotted the  $L_E$  measure against the X-ray temperature of the most X-ray luminous clusters at  $z \sim 0.2$ , and found a good correlation. This suggests that  $L_E$  may be a good tracer of cluster mass. Using the relation between velocity dispersion and X-ray temperature of Wu et al. (1999) to transform the Smail et al. (1998) data yields a power law fit which is consistent with our data, although given the large uncertainties on our velocity dispersions, we cannot constrain this relation. We simply note that given our limited data, we cannot tell if the relation between  $L_E$  and  $\sigma$  for X-ray luminous clusters still holds for X-ray underluminous systems.

Spectroscopic observations are underway for several of the XDCS clusters as part of other projects, and so these should allow much more accurate estimates of the velocity dispersions, further investigation of this relation, and the use of  $L_E$  as a mass estimator.

**Table 12.** Cluster velocity dispersion estimates. Columns are: ID of redshift grouping; Field ID; Number of galaxies (N) used in redshift determination; velocity dispersion ( $\sigma_z$ ); velocity dispersion in cluster rest-frame; and error on this quantity from jack-knife estimate (see text). This error estimate is likely to be biased in the presence of very small N (i.e.  $\sim 3$ ), and so such error estimates should be treated cautiously. Most of the more reliable systems show velocity dispersions in the range  $300 \text{ km s}^{-1} - 700 \text{ km s}^{-1}$ , typical of massive groups and low - intermediate mass clusters.

Grouping ID	Field	N	z	$\sigma_z$	$\sigma_z^{rest}$ ( $\text{km s}^{-1}$ )	$\Delta\sigma_z^{rest}$ ( $\text{km s}^{-1}$ )
1a	R110_1	3	0.196440	0.00031	78	95
2a	R220_2	7	0.259740	0.00143	341	346
3a	R236_1	6	0.297210	0.00315	728	504
3b	R236_1	11	0.347100	0.00179	398	262
4a	R294_1	3	0.268450	0.00259	612	750
4b	R294_1	3	0.325470	0.00224	506	620
4c	R294_1	5	0.453810	0.00467	962	1051

## 7.7 Summary of Spectroscopic Results

Spectroscopy has been undertaken for four XDCS subfields, containing cluster candidates not showing significant X-ray emission. Candidate groups in redshift space were identified, and the significance of these groups evaluated by three different techniques. The first two involved bootstrap resampling the Canada-France Redshift Survey using different selection functions. Using a simple magnitude limited selection showed (in general agreement with Holden et al. (1999)'s method) that 3 concurrent redshifts was a significant grouping; using a Gaussian magnitude selection greatly reduced the significance of these groups (showing the technique is very sensitive to the simulated selection function), but the drawbacks of both these techniques were discussed. An argument based on the space-density of early-type galaxies showed that three early-type galaxies constituted a robust group. Using this latter argument, one group was detected in each of two of the fields, and two groups were detected in the other two fields. The colour-magnitude finder correctly separated line of sight projected systems and also detected a higher redshift system, not revealed by the spectroscopy (most likely as galaxies sufficiently faint were not targeted). The CMR redshift error is around 0.04, for groups in the redshift range 0.2 - 0.4. Velocity dispersions for most of these systems are around  $300 - 700 \text{ km s}^{-1}$  (corresponding to massive groups and low - intermediate mass clusters) but these are estimated from tiny numbers of galaxies ( $\approx 5$ ), and have jack-knife estimated errors of around 60 - 100% (and for the systems with only 3 redshifts, these errors are likely to be underestimated). Finally, the luminosity in early-type galaxies versus the velocity dispersion was compared with the relation taken for the high X-ray luminosity cluster sample of Smail et al. (1998), and seen to be consistent, although the errors on the XDCS velocity dispersions are very large.

## 8 DISCUSSION, CONCLUSIONS & FUTURE WORK

The original motivation for this work was the studies of Bower et al. (1994) and Bower et al. (1997), which found that in an optically selected survey of galaxy clusters at  $z \sim 0.4$ , the X-ray emission was systematically lower than expected for a non-evolving X-ray luminosity function, relative to local samples. Their spectroscopic analysis indicated that these systems had velocity dispersions comparable to those of more X-ray luminous systems, which suggested that if the clusters were virialised then they had dynamical masses similar to the more X-ray luminous/ massive

systems; or that the systems were in fact unrelaxed and their velocity dispersions were thus inflated above that of a relaxed system.

This work has constructed similar optically selected samples, albeit from a smaller area ( $11 \text{ deg}^2$  versus  $27 \text{ deg}^2$ ) but with a more quantifiable selection function and using more efficient selection techniques. The relationship between X-ray luminosity and richness (as measured three different ways) shows considerable scatter.

During the course of this work, results from a similar study by Donahue et al. (2001) were published. They conducted an optical and X-ray survey in 23 deep ROSAT fields ( $4.8 \text{ deg}^2$ ) using Postman et al. 1996's Matched Filter algorithm on I-band data. The depth of their photometry was about 0.5 magnitudes deeper than that of the XDCS, although their areal coverage was lower by more than a factor of two. Donahue et al. (2001) detected 57 X-ray candidate clusters and 152 candidates in the optical. Their MF algorithm detected 74% (26 out of 35) of the most reliable X-ray candidates. This number is in good agreement with the 75% (9 out of 12) found with the MF algorithm used here. We have shown that an even higher recovery rate is possible using CMR techniques (potentially 10 out of 10) and with much more reliable redshift estimates.

As in Donahue et al. (2001), we find that within their optically selected sample, optical and X-ray luminosity are correlated, with considerable scatter. Their measure of richness is essentially the number of  $L^*$  galaxies ( $\Lambda$  in equation 5) contributing to the cluster signal at their MF estimated redshift. We show that the MF estimated redshifts are much poorer than those estimated from the CMR finder. This will potentially increase the scatter of the relation. They state that although there is significant scatter within the relation, there is no need to impose a bimodal distribution of X-ray luminous and X-ray faint clusters. This seems to be borne out by this work, as the distribution of detections in Fig. 18 appears continuous.

We find a scatter of 0.2 dex (a factor of 1.6) in the relation. Clearly this is important if all the systems (both X-ray dark and bright) are needed for cosmological models. Our X-ray dark clusters are certainly convincing and in §7 we show that they are confirmed by spectroscopy. How we deal with the scatter in cosmological surveys depends on its origin. We consider this below.

Possible reasons for this scatter include:

1) Variations in the efficiency of galaxy formation. If galaxy formation is more efficient at a given epoch/ environment, then for a given mass of gas, a higher fraction can be converted to stars, increasing the light to mass ratio of a cluster. Furthermore, this leaves less gas available for production of X-ray emission, decreasing the X-ray luminosity. So, higher galaxy formation efficiency leads to increased optical luminosity and decreased X-ray luminosity. This, however, is not seen in semi-analytic galaxy formation models such as Cole et al. (2000).

2) The dynamical state of the cluster. As mentioned before, if a cluster is dynamically unrelaxed then the hot intracluster gas will not be centrally concentrated to densities sufficient for X-ray emission (§1). If the cluster galaxies are already in place (as seems to be suggested by Stanford et al. 2001) then such a cluster would have an unusually low X-ray luminosity for its optical luminosity. High resolution observations with Chandra have shown cluster cores are far from relaxed (Mazzotta et al. 2001) but what we require here is an even more widespread distribution of X-ray properties.

3) Thermal history of the gas. The presence of cooling gas in the cluster raises the ICM density and initially increases X-ray luminosity. Conversely, injecting energy into the ICM at early times [e.g. by AGN or through supernovae/ feedback from galaxy formation (Ponman et al. 1999; Wu et al. 1998; Voit et al. 2002;

Bower et al. 2001)] decreases the ICM density and lowers X-ray luminosity. Both these effects could contribute to scatter in the optical – X-ray luminosity relation. The scatter may also reflect different levels of preheating from cluster to cluster (Mushotzky & Scharf 1997).

4) Projection effects. Groups of galaxies projected along the line of sight would appear as higher optical luminosity clusters (since the number of galaxies observed is simply additive); whereas the X-ray luminosity would appear extremely low for a cluster of such optical richness, as the X-ray luminosity scales as the square of the gas density. This was shown to probably not be a significant factor in §6, by separately considering optical cluster candidates flagged as projections. Although, again, the volume probed by this survey is relatively small, so large scale filaments viewed ‘end-on’ may be too rare to be included.

These mechanisms all assume that the fundamental parameter is the cluster mass. The best measurement for the cluster mass in this paper is the velocity dispersion. This suggested that within the (large) errors, a sample of optically selected, X-ray underluminous clusters had optical luminosities consistent with those of the most X-ray luminous clusters. Clearly, better mass estimates are required for a larger number of clusters. Recently, Yee & Ellingson (2003) have examined the CNOC1 sample of X-ray luminous clusters, and found that  $B_{gc}$ ,  $T_X$  and  $L_X$  can be used to infer the dynamical mass of these systems to within 30%. Other possible mass estimators include gravitational lensing (Hoekstra et al. 2002) or total K-band galaxy luminosity (Lin et al. 2003).

## ACKNOWLEDGEMENTS

Based on observations made with the Isaac Newton Telescope operated on the island of La Palma by the Isaac Newton Group in the Spanish Observatorio del Roque de los Muchachos of the Instituto de Astrofísica de Canarias.

We thank the referee, M. Gladders, for a careful reading which improved the clarity of this manuscript.

The authors acknowledge useful discussions with Alastair Edge, Mike Gladders, Mike Irwin, Laurence Jones, Catarina Lobo, Pasquale Mazzotta, Nigel Metcalfe, Ray Sharples, Ian Smail, and Alexey Vikhlinin. Thanks for technical help with various stages of this project go to Mike Balogh, Eric Bell, Harald Kuntschner, and Peder Norberg; and to Taddy Kodama for providing results of his stellar population synthesis models.

Particular thanks go to Peter Draper and Mark Taylor for assistance with the WFC distortion correction.

We are grateful to the staff of the ING and Calar Alto observatories for assistance with the observations presented here. DGG is supported by the Leverhulme Trust and was supported by a PPARC studentship for the bulk of this work. BLZ acknowledges financial support from the Volkswagen Foundation (I/76520) and the Deutsche Forschungsgemeinschaft (ZI 663/2–1).

## REFERENCES

- Abell, G. O. 1958, *ApJS*, 3, 211+
- Abell, G. O., Corwin, H. G., & Olowin, R. P. 1989, *ApJS*, 70, 1
- Allen, S. W. & Fabian, A. C. 1998, *MNRAS*, 297, L63
- Andersen, V. & Owen, F. N. 1994, *AJ*, 108, 361
- Arnaud, M. & Evrard, A. E. 1999, *MNRAS*, 305, 631
- Bahcall, N. A. 1981, *ApJ*, 247, 787
- Bartelmann, M. 1996, *A&A*, 313, 697
- Beers, T. C., Flynn, K., & Gebhardt, K. 1990, *AJ*, 100, 32
- Bertin, E. & Arnouts, S. 1996, *A&AS*, 117, 393
- Bower, R. G., Benson, A. J., Lacey, C. G., Baugh, C. M., Cole, S., & Frenk, C. S. 2001, *MNRAS*, 325, 497
- Bower, R. G., Bohringer, H., Briel, U. G., Ellis, R. S., Castander, F. J., & Couch, W. J. 1994, *MNRAS*, 268, 345+
- Bower, R. G., Castander, F. J., Ellis, R. S., Couch, W. J., & Bohringer, H. 1997, *MNRAS*, 291, 353+
- Bower, R. G., Lucey, J. R., & Ellis, R. S. 1992, *MNRAS*, 254, 601+
- Carlberg, R. G., Yee, H. K. C., Ellingson, E., Abraham, R., Gravel, P., Morris, S., & Pritchet, C. J. 1996, *ApJ*, 462, 32+
- Carlberg, R. G., Yee, H. K. C., Ellingson, E., Morris, S. L., Abraham, R., Gravel, P., Pritchet, C. J., Smecker-Hane, T., Hartwick, F. D. A., Hesser, J. E., Hutchings, J. B., & Oke, J. B. 1997, *ApJ*, 485, L13
- Cash, W. 1979, *ApJ*, 228, 939
- Castander, F. J., Bower, R. G., Ellis, R. S., Aragon-Salamanca, A., Mason, K. O., Hasinger, G., McMahon, R. G., Carrera, F. J., Mittaz, J. P. D., Perez-Fournon, I., & Lehto, H. J. 1995, *Nature*, 377, 39
- Castander, F. J., Ellis, R. S., Frenk, C. S., Dressler, A., & Gunn, J. E. 1994, *ApJ*, 424, L79
- Cole, S., Lacey, C. G., Baugh, C. M., & Frenk, C. S. 2000, *MNRAS*, 319, 168
- Colless, M. 1989, *MNRAS*, 237, 799
- Couch, W. J., Ellis, R. S., MacLaren, I., & Malin, D. F. 1991, *MNRAS*, 249, 606
- Davis, M. & Peebles, P. J. E. 1983, *ApJ*, 267, 465
- Donahue, M., Mack, J., Scharf, C., Lee, P., Postman, M., Rosati, P., Dickinson, M., Voit, G. M., & Stocke, J. T. 2001, *ApJ*, 552, L93
- Dressler, A. 1980, *ApJS*, 42, 565
- Efron, B. 1982, *The Jackknife, the Bootstrap and Other Resampling Plans* (Philadelphia: SIAM)
- Eke, V. R., Cole, S., & Frenk, C. S. 1996, *MNRAS*, 282, 263
- Gal, R. R., de Carvalho, R. R., Odewahn, S. C., Djorgovski, S. G., & Margoniner, V. E. 2000, *AJ*, 119, 12
- Gilbank, D. G. 2001, PhD Thesis, University of Durham
- Gladders, M. D. & Yee, H. K. C. 2000, *AJ*, 120, 2148
- Gunn, J. E., Hoessel, J. G., & Oke, J. B. 1986, *ApJ*, 306, 30
- Hill, G. J. & Lilly, S. J. 1991, *ApJ*, 367, 1
- Hoekstra, H., Franx, M., Kuijken, K., & van Dokkum, P. G. 2002, *MNRAS*, 333, 911+
- Holden, B. P., Nichol, R. C., Romer, A. K., Metevier, A., Postman, M., Ulmer, M. P., & Lubin, L. M. 1999, *AJ*, 118, 2002
- Huchra, J. P. & Geller, M. J. 1982, *ApJ*, 257, 423
- Jones, L. R., Ponman, T. J., & Forbes, D. A. 2000, *MNRAS*, 312, 139
- Jones, L. R., Ponman, T. J., Horton, A., Babul, A., Ebeling, H., & Burke, D. J. 2003, *ArXiv Astrophysics e-prints*, 4257
- Jones, L. R., Scharf, C., Ebeling, H., Perlman, E., Wegner, G., Malkan, M., & Horner, D. 1998, *ApJ*, 495, 100+
- Katgert, P., Mazure, A., Perea, J., den Hartog, R., Moles, M., Le Fevre, O., Dubath, P., Focardi, P., Rhee, G., Jones, B., Escalera, E., Biviano, A., Gerbal, D., & Giuricin, G. 1996, *A&A*, 310, 8
- Kawasaki, W., Shimasaku, K., Doi, M., & Okamura, S. 1998, *A&AS*, 130, 567
- Kepner, J., Fan, X., Bahcall, N., Gunn, J., Lupton, R., & Xu, G. 1999, *ApJ*, 517, 78
- Kodama, T. & Arimoto, N. 1997, *A&A*, 320, 41

- Kodama, T., Arimoto, N., Barger, A. J., & Arag'ón-Salamanca, A. 1998, *A&A*, 334, 99
- Landolt, A. U. 1992, *AJ*, 104, 340
- Lilly, S. J., Cowie, L. L., & Gardner, J. P. 1991, *ApJ*, 369, 79
- Lilly, S. J., Le Fevre, O., Crampton, D., Hammer, F., & Tresse, L. 1995, *ApJ*, 455, 50
- Lin, H., Yee, H. K. C., Carlberg, R. G., Morris, S. L., Sawicki, M., Patton, D. R., Wirth, G., & Shepherd, C. W. 1999, *ApJ*, 518, 533
- Lin, Y., Mohr, J. J., & Stanford, S. A. 2003, *ArXiv Astrophysics e-prints*, 4033
- Lobo, C., Iovino, A., Lazzati, D., & Chincarini, G. 2000, *A&A*, 360, 896
- Longair, M. S. & Seldner, M. 1979, *MNRAS*, 189, 433
- Lubin, L. M. & Postman, M. 1996, *AJ*, 111, 1795+
- Lucey, J. R., 1983, *MNRAS*, 204, 33
- Lumsden, S. L., Nichol, R. C., Collins, C. A., & Guzzo, L. 1992, *MNRAS*, 258, 1
- Maddox, S. J., Efstathiou, G., & Loveday, J. 1988, in *IAU Symp. 130: Large Scale Structures of the Universe*, Vol. 130, 151+
- Markevitch, M. 1998, *ApJ*, 504, 27
- Mason, K. O., Carrera, F. J., Hasinger, G., Andernach, H., Aragon-Salamanca, A., Barcons, X., Bower, R., Brandt, W. N., Branduardi-Raymont, G., Burgos-Martín, J., Cabrera-Guerra, F., Carballo, R., Castander, F., Ellis, R. S., González-Serrano, J. I., Martínez-González, E., Martín-Mirones, J. M., McMahon, R. G., Mittaz, J. P. D., Nicholson, K. L., Page, M. J., Pérez-Fournon, I., Puchnarewicz, E. M., Romero-Colmenero, E., Schwobe, A. D., Vila, B., Watson, M. G., & Wonnacott, D. 2000, *MNRAS*, 311, 456
- Mazzotta, P., Markevitch, M., Vikhlinin, A., Forman, W. R., David, L. P., & VanSpeybroeck, L. 2001, *ApJ*, 555, 205
- Metcalf, N., Shanks, T., Campos, A., McCracken, H. J., & Fong, R. 2001, *MNRAS*, 323, 795
- Miller, N. A., Owen, F. N., Burns, J. O., Ledlow, M. J., & Voges, W. 1999, *AJ*, 118, 1988
- Mitchell, R. J., Culhane, J. L., Davison, P. J. N., & Ives, J. C. 1976, *MNRAS*, 175, 29P
- Mushotzky, R. F. & Scharf, C. A. 1997, *ApJ*, 482, L13+
- Navarro, J. F., Frenk, C. S., & White, S. D. M. 1997, *ApJ*, 490, 493+
- Nichol, R. C., Holden, B. P., Romer, A. K., Ulmer, M. P., Burke, D. J., & Collins, C. A. 1997, *ApJ*, 481, 644+
- Ponman, T. J., Allan, D. J., Jones, L. R., Merrifield, M., McHardy, I. M., Lehto, H. J., & Luppino, G. A. 1994, *Nature*, 369, 462+
- Ponman, T. J., Cannon, D. B., & Navarro, J. F. 1999, *Nature*, 397, 135
- Postman, M., Lubin, L. M., Gunn, J. E., Oke, J. B., Hoessel, J. G., Schneider, D. P., & Christensen, J. A. 1996, *AJ*, 111, 615+
- Ramella, M., Biviano, A., Boschin, W., Bardelli, S., Scodreggio, M., Borgani, S., Benoist, C., da Costa, L., Girardi, M., Nonino, M., & Olsen, L. F. 2000, *A&A*, 360, 861
- Reichart, D. E., Castander, F. J., & Nichol, R. C. 1999, *ApJ*, 516, 1
- Romer, A. K., Nichol, R. C., Holden, B. P., Ulmer, M. P., Pildis, R. A., Merrelli, A. J., Adami, C., Burke, D. J., Collins, C. A., Metevier, A. J., Kron, R. G., & Commons, K. 2000, *ApJS*, 126, 209
- Schechter, P. 1976, *ApJ*, 203, 297
- Serlemitsos, P. J., Smith, B. W., Boldt, E. A., Holt, S. S., & Swank, J. H. 1977, *ApJ*, 211, L63
- Smail, I., Edge, A. C., Ellis, R. S., & Blandford, R. D. 1998, *MNRAS*, 293, 124+
- Smail, I., Hogg, D. W., Yan, L., & Cohen, J. G. 1995, *ApJ*, 449, L105
- Soneira, R. M. & Peebles, P. J. E. 1978, *AJ*, 83, 845
- Stanford, S. A., Holden, B., Rosati, P., Tozzi, P., Borgani, S., Eisenhardt, P. R., & Spinrad, H. 2001, *ApJ*, 552, 504
- Tonry, J. & Davis, M. 1979, *AJ*, 84, 1511
- van Haarlem, M. P., Frenk, C. S., & White, S. D. M. 1997, *MNRAS*, 287, 817
- Vikhlinin, A., McNamara, B. R., Forman, W., Jones, C., Quintana, H., & Hornstrup, A. 1998, *ApJ*, 502, 558+
- Visvanathan, N. 1978, *A&A*, 67, L17
- Voit, G. M., Bryan, G. L., Balogh, M. L., & Bower, R. G. 2002, *ApJ*, 576, 601
- Williams, J. P., de Geus, E. J., & Blitz, L. 1994, *ApJ*, 428, 693
- Wittman, D., Tyson, J. A., Margoniner, V. E., Cohen, J. G., & Dell'Antonio, I. P. 2001, *ApJ*, 557, L89
- Wu, K. K. S., Fabian, A. C., & Nulsen, P. E. J. 1998, *MNRAS*, 301, L20
- Wu, X., Xue, Y., & Fang, L. 1999, *ApJ*, 524, 22
- Yee, H. K. C. & Green, R. F. 1987, *ApJ*, 319, 28
- Yee, H. K. C. & López-Cruz, O. 1999, *AJ*, 117, 1985
- Yee, H. K. C., Morris, S. L., Lin, H., Carlberg, R. G., Hall, P. B., Sawicki, M., Patton, D. R., Wirth, G. D., Ellingson, E., & Shepherd, C. W. 2000, *ApJS*, 129, 475
- Yee, H. K. C. & Ellingson, E. 2003, *ApJ*, 585, 215
- Zwicky, F. & et al. 1968, in *California Inst. Techn.*, 4 (1968), 0+